Rheology of a suspension of deformable spheres in a weakly viscoelastic fluid

Liam J Escott[1], Helen J Wilson*

[a]*Department of Mathematics, UCL, Gower Street, WC1E 6BT, London, UK*

Abstract

In this work, we consider a suspension of weakly deformable solid particles within a weakly viscoelastic fluid. The fluid phase is modelled as a second-order fluid, and particles within the suspended phase are assumed linearly elastic and relatively dilute. We apply a cell model as a proxy for mean field flow, and solve analytically within a cellular fluid layer and its enclosed particle. We use an ensemble averaging process to derive analytical results for the bulk stress in suspension, and evaluate the macroscopic properties in both shear and extensional flow. Our viscometric functions align with existing literature over a surprisingly broad range of fluid and solid elasticities.

The suspension behaves macroscopically as a second-order fluid, and we give simple formulae by which the reader can calculate the parameters of this effective fluid, for use in more complex simulations. We additionally calculate the particle shape and orientation, and in simple shear flow show that the leading-order modifications to the angle of inclination ζ act to align the particle towards the flow direction, giving $\zeta = \pi/4 - 3Ca_\mathrm{e}/4 + \alpha_0 Wi/2\alpha_1$ where Ca_e is the elastic capillary number, Wi is the Weissenberg number, and α_i are material properties of the suspending second-order fluid, for which the ratio α_0/α_1 is negative.

Keywords: Dilute suspension; second-order fluid; elastic solid; cell model; solid-fluid interactions; constitutive model; angle of inclination.

---

*Corresponding author: `helen.wilson@ucl.ac.uk`

[1] Current address: `escottl@aston.ac.uk`

---

1. Introduction

Suspensions of deformable particles are very commonly found in nature, some examples being blood, paint, slurries, molten lava and a variety of pharmaceutical products. It is not uncommon for the elasticity of suspended phase to be non-negligible, even when particles are extremely small. The study of these materials has taken place for over a century, and there is still a real need for simple constitutive equations which describe their motion and characteristics in bulk.

Even the simpler situation of rigid solid particles suspended in a Newtonian background flow, which has been studied extensively, shows complex behaviour. Experimental systems are known to exhibit both shear-thickening and shear-thinning behaviour (Bergström, 1998). Shear-thickening is understood to be a consequence of inter-particle contacts and friction (e.g. Fernandez et al., 2013, Wyart and Cates, 2014, Seto et al., 2017), eventually leading to jamming of the suspension (Liu and Nagel, 2001). Shear-thinning, on the other hand, occurs primarily in suspensions of weakly attracting particles, and has been attributed to the breakdown of particle clusters under imposed flow (Xu et al., 2013).

The effective viscosity of such suspensions has been a topic of interest for many years. The first correction to viscosity induced by the presence of the solid particles was derived by Einstein (1906); the well-known "Einstein viscosity" $\eta_{\text{eff}} = \eta_0(1 + 5\phi/2)$, where η_0 is the viscosity of the Newtonian solvent fluid. This expression precisely describes the suspension behaviour in the dilute limit, where ϕ, the volume fraction of solids, is small. Further work to extend this relationship was conducted by Batchelor and Green (1972), who calculated an approximate $O(\phi^2)$ correction to the viscosity via the use of hydrodynamic functions $J(r)$ and $q(r)$ which they introduced. While this correction does extend the range of concentration past dilute, it is known that many-body effects (including jamming) will become dominant after a relatively small increase in ϕ.

There is also a substantial body of work on suspensions of non-spherical particles in a Newtonian fluid. Jeffery (1922) provided the seminal work in the area, deriving the rotation of the principal angles of a solid ellipsoid in shear flow. The effective viscosity in a dilute suspension of such particles, assuming a homogeneous velocity profile within the solid phase, was derived simultaneously by Roscoe (1967) and Goddard and Miller (1967). Since then, the understanding of these materials has been substantially understood via a range of numerical techniques (by, e.g., Ardekani and Rangel, 2008, Le et al., 2006, Pozrikidis, 1992), both the flow in the vicinity of a single inclusion and the behaviour of the suspension in bulk.

The effort to introduce viscoelasticity into the Einstein viscosity relation has been long and complex (see, for example Kaloni and Statsna, 1983, Mifflin, 1985, Patankar and Hu, 2001, Greco et al., 2007, Housiadas and Tanner, 2009, all of which address the question of rigid spheres in a second-order fluid in the dilute limit). The correct analysis was eventually provided by Koch and Subramanian (2006, 2008) and later confirmed by Rallison (2012). These most recent papers provide expressions for the first and second normal stress differences, as well as viscosity, correct to order ϕ for a dilute suspension; they reduce to the expected Newtonian quantities as the Weissenberg number $Wi \to 0$.

Beyond the purely dilute limit, the current understanding of rigid-particle suspensions in viscoelastic fluids is based on a combination of experiments and numerical simulations. Experimentally, Dai et al. (2014) provided a thorough assessment of the behaviour of rigid spheres suspended in a Boger fluid for a wide range of solid volume fractions. Early two-dimensional simulations of startup flows by Jaensson et al. (2015) showed that viscoelasticity can drive particles to align in strings along the flow direction at moderate concentrations, providing the Weissenberg number is sufficiently high (above 1). This observation is coupled with a reduction in viscosity because of the particle alignment, and an increase in first normal stress difference. More recently, a series of fully three-dimensional numerical studies by Yang and co-authors (Yang et al., 2016, Yang and Shaqfeh, 2018a,b) predict a positive first normal stress difference, and negative second normal stress difference. They separate out the extra stress due to the particles into two contributions: the stresslet and the particle-induced fluid stress, which often act in competition with one another.

Everything we have discussed so far pertains to rigid particles. However, the particles found in a wide variety of natural processes can be deformed by the flow, and the behaviour of such suspensions is not necessarily well captured using an assumption of rigid behaviour.

We will first look at the flow of a Newtonian fluid around a deformable particle. This general field has applications to capsule dynamics (e.g. Clausen and Aidun, 2010, Matsunaga et al., 2016) and red blood cells (e.g. Chien, 1987, Barthès-Biesel, 1980, Barthès-Biesel and Rallison, 1981, Keller and Skalak, 1982).

Often the change in shape of the suspended phase, whether in steady or unsteady flow, can be modelled by introducing elasticity to the particle. The first theoretical work using elastic particles is by Fröhlich and Sack (1946), who looked at the situation of an applied extensional stress, and found flow solutions for flow around an elastic sphere in the limit of small surface deformation. Using a slightly different set of modelling assumptions, Murata (1981) considered a wider variety of imposed flows around an elastic particle whose shape remains almost spherical: this work assumed that the particle surface remains steady in time (a *tank-treading* motion). All these works consider a single particle, and so produce information appropriate to dilute systems. More recent work includes experimental studies such as Adams et al. (2004), which found the deformability of the particles could generate a shear-thinning viscosity; and a number of computational studies. Several of these (e.g. Zhang et al., 2004, Zhang and Gay, 2007, Gao and Hu, 2009, Villone et al., 2014) investigate the viscometric functions in dilute systems; and even more recently Rosti et al. (2018) has made progress towards the behaviour of the effective viscosity of a suspension of deformable particles at higher than dilute concentrations. There are also a range of more specific computational works, which, rather than trying to capture suspension rheology, model specific applications such as microfluidics (e.g. Villone et al., 2019, Villone, 2019), showing the wide applicability of suspension mechanics even in complex systems.

As we have seen, there is substantial literature on rigid and deformable particles in a Newtonian fluid, and on rigid particles in viscoelastic fluids. However, despite its industrial relevance, there is little work which considers deformable particles in a viscoelastic fluid. Hwang et al. (2004) and Malidi and Harlen (2008) both carried out simulations of a very small number of deformable particles (1–3) in two dimensions in an Oldroyd-B or Pompom suspending fluid, while Guido and Shaqfeh (2019) have carried out fully three-dimensional simulations of a single particle (in a periodic box) in shear flow, and deduced the rheology of the whole suspension. As yet, no-one has produced an analytical expression to approximate the suspension rheology for such a system.

In this paper we use a mean-field approximation via a cell model, alongside regular perturbation expansions, to construct a model of a suspension in which both weak viscoelastic effects and weak deformation effects are present. As we will see later, the validity of our model is limited to low-concentration suspensions, but we produce a constitutive model which is simple to implement numerically and can therefore be used in simulations of complex flows.

As an example, recent experimental work (Amini et al., 2022) has demonstrated that in real flows, highly non-uniform particle distributions can form leading to flow instabilities. To understand the mechanisms of such behaviour will require investigations built on a foundation of simple continuum models, so that complex interactions between volume fraction, rheology and flow can be understood.

In section 2 we introduce the governing equations and boundary conditions in both fluid and elastic solid phases, our methods of constructing average suspension behaviour, and the solution technique. Section 3 gives the results for the fluid flow, while in section 4 we show results on the particle deformation. These allow us to draw conclusions about the rheology of the suspension as a whole (section 5) producing an effective model of the whole suspension as a homogeneous second-order fluid. We finish with concluding remarks in section 6.

2. System of equations

2.1. Cell model

In this work we use a cell model to approximate the interactions between individual solid particles. This paradigm was introduced by Simha (1952) and Happel (1957). Sherwood (2006) carried out a careful analysis of the difference between these two works, elucidating the influence of the choice of which of the flow quantities (fluid velocity, tangential stress, normal stress) should be continuous across the cell boundary. We used the paradigm in our earlier work (Escott and Wilson, 2020) to produce a simple constitutive model for a suspension of rigid solid spheres in a second-order fluid.

The cell concept is essentially a mean-field approximation to suspension mechanics: each included particle is assigned a volume of fluid which surrounds it, and within which its modifications to the fluid flow are confined. At the outer edge of the cell, the velocity field is forced to match with an imposed background flow, while within the cell the fluid adapts to the presence of the particle. With this simplification, we can use a single fluid cell as an exemplar for all fluid cells, and therefore deduce (an approximation to) the full suspension behaviour without needing to consider particle interactions directly. Changing the volume of fluid assigned to each particle gives a proxy for altering the solid volume fraction, allowing us to go beyond the fully dilute asymptotic limit.

Some caution is required in applying the cell model approach to suspensions which have solid volume fractions beyond the dilute regime. There are three fundamental limitations to the model: the outer cell boundary is unphysical in the sense that there is a discontinuity in velocity gradients and in stress across it; the spherical shape of the cell means that the influence of neighbouring particles is felt uniformly over the whole particle surface; and, as we will see later, there is no solid theoretical foundation for a choice of cell size. All of these are of minor or no importance in very dilute systems, where the cell is large and any effects from the outer boundary are minimal. However, for higher volume fractions the appropriate cell size is smaller, and any inaccuracies relating to the behaviour at the outer cell boundary become more important. At very high volume fractions, true inter-particle effects such as contact and friction become important, and these cannot be captured by our mean-field approximation.

2.2. Governing equations

The governing equations for the fluid phase, which is an incompressible, inertialess second-order fluid, are those of mass and momentum conservation and the constitutive law:

$$\nabla \cdot \mathbf{v} = 0, \qquad \nabla \cdot \boldsymbol{\sigma} = 0, \tag{1}$$

$$\boldsymbol{\sigma} = -p\mathbf{I} + 2\eta_0 \mathbf{E} + \alpha_0 \mathbf{A} + 4\alpha_1 \mathbf{E} \cdot \mathbf{E}, \tag{2}$$

in which $\mathbf{v}$ and $\boldsymbol{\sigma}$ are the fluid velocity and stress respectively and p the pressure. Here $\mathbf{E} = \frac{1}{2}(\mathbf{L} + \mathbf{L}^\top)$ is the rate of strain tensor and $\mathbf{A}$ the second Rivlin–Ericksen tensor (Rivlin and Ericksen, 1955), defined in steady flows as

$$A_{ij} = 2\left(v_k \nabla_k E_{ij} + L_{ki} E_{kj} + E_{ik} L_{kj}\right). \tag{3}$$

We are using the convention $L_{ij} = \partial v_i / \partial x_j$ for the flow gradient tensor $\mathbf{L}$.

In the solid phase, we introduce the solid velocity $\overline{\mathbf{v}}$ and Lagrange pressure l, along with the stress tensor $\overline{\boldsymbol{\sigma}}$; we will also need a displacement vector $\mathbf{h}$. This is defined as the vector connecting an Eulerian point $\mathbf{x}$ inside or on the original elastic sphere, to its position after deformation due to the background flow: thus for a point $\mathbf{x}$ which originated from undeformed position $\mathbf{x}^0$ we have $\mathbf{x} = \mathbf{x}^0 + \mathbf{h}(\mathbf{x}^0)$. This can be seen for a point on the particle surface in figure 1.

We make the assumption here that the shape of the particle (as viewed by an observer in the laboratory frame) is constant in time. This is self-evident if the imposed flow has no rotational component; but in a shear flow it corresponds to an assumption that the motion is *tank-treading* rather than *tumbling*. For nonspherical rigid particles in a Stokes flow we know that tumbling motion occurs (Jeffery, 1922, Bretherton, 1962) but some numerical simulations do predict tank-treading for deformable particles in a viscoelastic environment (e.g. Malidi and Harlen, 2008) and this allows us to calculate steady stresses rather than averaging over a tumbling cycle.

With this assumption, the displacement vector is a steady, position-dependent quantity; if the particle shape is preserved (e.g. in a rigid body rotation) we have $\mathbf{h} = \mathbf{0}$. The solid velocity is related to this displacement via the material derivative:

$$\overline{\mathbf{v}} = \frac{D\mathbf{h}}{Dt}. \tag{4}$$

The equations governing the evolution of the solid velocity are conservation of mass and momentum as in the fluid phase:

$$\nabla \cdot \overline{\mathbf{v}} = 0, \qquad \nabla \cdot \overline{\boldsymbol{\sigma}} = \mathbf{0}. \tag{5}$$

For the constitutive model, we limit our analysis to small deformations, and to minimise complexity we use a linearly elastic, Hookean model (Howell et al., 2009) with an isotropic elastic modulus:

$$\overline{\boldsymbol{\sigma}} = -l\mathbf{I} + 2\mu\mathbf{e}, \tag{6}$$

in which we have introduced the displacement gradient tensor $\mathbf{e} = \frac{1}{2}(\nabla\mathbf{h} + \nabla\mathbf{h}^\top)$. This model is appropriate for small deformations such that the dimensionless quantity $\nabla\mathbf{h}$ is small in absolute terms; all of $\mathbf{h}$, $\mathbf{e}$ and $\overline{\boldsymbol{\sigma}}$ are small quantities in our analysis. The quantity μ is the shear elastic modulus.

Finally, the evolution equation for the solid strain tensor $\mathbf{e}$ is:

$$\frac{D\mathbf{e}}{Dt} + \mathbf{e} \cdot \overline{\mathbf{L}} + \overline{\mathbf{L}}^\top \cdot \mathbf{e} = \frac{1}{2}\left(\overline{\mathbf{L}} + \overline{\mathbf{L}}^\top\right), \tag{7}$$

in which the solid velocity gradient $\overline{\mathbf{L}}$ is defined as $\overline{L}_{ij} = \partial\overline{v}_i/\partial x_j$. This is equivalent to the evolution equation for the Eulerian Almanski strain tensor as derived in Gao and Hu (2009), after neglecting quadratic terms in the deformation gradient.

2.3. Boundary conditions

Outside the fluid cell, we impose a general linear background flow $\mathbf{v}^{\infty} = \mathbf{E}^{\infty} \cdot \mathbf{x} + \mathbf{\Omega}^{\infty} \cdot \mathbf{x}$, with $\mathbf{E}^{\infty}$ (symmetric) and $\mathbf{\Omega}^{\infty}$ (antisymmetric) the constant far-field rate of strain tensor and rotation rate tensor respectively.

At the outer boundary $r = R_0 b$ of the fluid cell around a particle of radius R_0 centred on the origin, we match this to the true fluid velocity:

$$\mathbf{v}\left(R_0 b\right) = R_0 b \mathbf{E}^{\infty} \cdot \hat{\mathbf{n}} + R_0 b\, \mathbf{\Omega}^{\infty} \cdot \hat{\mathbf{n}} \tag{8}$$

in which we have introduced for any point $\mathbf{x}$ its magnitude r and unit vector $\hat{\mathbf{n}} = \mathbf{x}/r$.

Next we enforce the condition that the interface between the fluid and the (slightly deformed) particle is a material surface: that is, points which start on the interface remain on the interface.

Consider a point $\mathbf{x}$ which is fixed in space, on the surface of the deformed sphere. There is a constant flux of material elements through this point, but at each time instant the point is occupied by a material element which would relax to the *same* physical point $\mathbf{x}^0$ on the surface of the undeformed sphere.

Suppose we represent the angular position of the point $\mathbf{x}$ by the ordered pair $\boldsymbol{\chi} = \{\theta, \varphi\}$ containing its polar and azimuthal angles (from spherical polar coordinates). Then we can parameterise the material surface using the angular position where each point belongs on the undeformed sphere, which we denote $\boldsymbol{\chi}^{0,1}$; its position on the deformed surface will have angular position $\boldsymbol{\chi}^1$. This is represented schematically in figure 1, along with the unit normal $\hat{\mathbf{N}}$ to the solid surface, which has been perturbed from its rigid value $\hat{\mathbf{n}}$ by the fluid flow.

We also represent the boundary by the polar equation

$$r = R_0 \left[1 + \Delta\left(\boldsymbol{\chi}\right)\right] \tag{9}$$

and we need to calculate the radial displacement of the surface, Δ. Any point within the solid particle can be written in terms of its relaxed position within the undeformed particle,

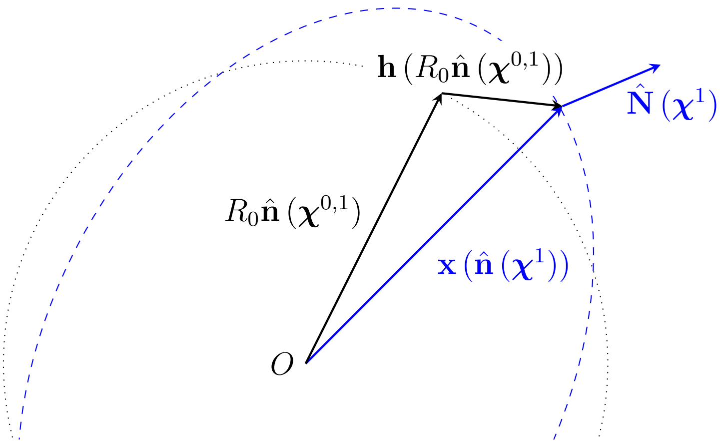

Figure 1: The relationship between current position $\mathbf{x}$ of a material surface element and its previous position on the undeformed particle surface. The blue dashed line represents the current deformed shape, modified from its original spherical shape (dotted black line). $\boldsymbol{\chi} = \{\theta, \varphi\}$ is an ordered pair containing the angular values of position. The position $\mathbf{x}$ at current angle $\boldsymbol{\chi}^1$ is described in terms of its original angle $\boldsymbol{\chi}^{0,1}$ and displacement $\mathbf{h}$.

$\mathbf{x}^0$, as $\mathbf{x} = \mathbf{x}^0 + \mathbf{h}(\mathbf{x}^0)$. The property that distinguishes points on the surface is that $|\mathbf{x}^0| = R_0$: that is, $|\mathbf{x} - \mathbf{h}(\mathbf{x}^0)| = R_0$. Expressing our points in terms of their angular parameterisation gives the condition for a material surface:

$$\left|\mathbf{x}\left(\boldsymbol{\chi}^1\right) - \mathbf{h}\left(R_0\boldsymbol{\chi}^{0,1}\right)\right| = R_0 \quad \text{at} \quad r = R_0\left[1 + \Delta\left(\boldsymbol{\chi}^1\right)\right], \tag{10}$$

which will be sufficient information to calculate Δ.

Having defined the fluid–solid interface, we can now impose the usual interfacial equations: no penetration of the fluid into the solid (using $\hat{\mathbf{N}}$ as defined above):

$$\mathbf{v} \cdot \hat{\mathbf{N}} = 0 \quad \text{at} \quad r = R_0\left(1 + \Delta\right); \tag{11}$$

velocity matching between fluid and solid:

$$\overline{\mathbf{v}} = \mathbf{v} \quad \text{at} \quad r = R_0\left(1 + \Delta\right); \tag{12}$$

and matching of traction between the solid and fluid phase:

$$\overline{\boldsymbol{\sigma}} \cdot \hat{\mathbf{N}} = \boldsymbol{\sigma} \cdot \hat{\mathbf{N}} \quad \text{at} \quad r = R_0\left(1 + \Delta\right). \tag{13}$$

Finally, we require that both l and $\mathbf{h}$ are finite at the cell and particle origin $r = 0$.

2.4. Non-dimensionalisation

We choose as our length scale the undeformed particle radius R_0, and as our timescale the inverse of the generalised shear rate $||\mathbf{E}^\infty|| = \left(2\mathbf{E}^\infty : \mathbf{E}^\infty\right)^{1/2}$. Stresses in the fluid are scaled using the solvent viscosity η_0 and those in the solid with the elastic modulus μ.

In terms of new dimensionless variables, the governing equations become, for the fluid:

$$\nabla \cdot \mathbf{v} = 0, \qquad \nabla \cdot \boldsymbol{\sigma} = \mathbf{0}, \qquad \boldsymbol{\sigma} = -p\mathbf{I} + 2\mathbf{E} + Wi\left(\epsilon\mathbf{A} + 4\mathbf{E}\cdot\mathbf{E}\right), \tag{14}$$

and for the solid:

$$\nabla \cdot \overline{\mathbf{v}} = 0, \qquad \nabla \cdot \overline{\boldsymbol{\sigma}} = \mathbf{0}, \qquad \overline{\boldsymbol{\sigma}} = -l\mathbf{I} + 2\mathbf{e}, \tag{15}$$

with unchanged equations for the remaining variables:

$$\mathbf{A} = 2\left(\mathbf{v}\cdot\nabla\mathbf{E} + \mathbf{L}^\top\cdot\mathbf{E} + \mathbf{E}\cdot\mathbf{L}\right), \qquad \frac{D\mathbf{e}}{Dt} - \overline{\mathbf{L}}\cdot\mathbf{e} - \mathbf{e}\cdot\overline{\mathbf{L}}^\top = \frac{1}{2}\left(\overline{\mathbf{L}} + \overline{\mathbf{L}}^\top\right). \tag{16}$$

The boundary conditions become, on the outer cell boundary:

$$\mathbf{v} = b\,\mathbf{E}^\infty\cdot\mathbf{n} + b\,\boldsymbol{\Omega}^\infty\cdot\mathbf{n} \qquad \text{on } r = b; \tag{17}$$

the material interface condition at the surface of the sphere:

$$\left|\left(1 + \Delta\left(\boldsymbol{\chi}^1\right)\right)\hat{\mathbf{n}}\left(\boldsymbol{\chi}^1\right) - \mathbf{h}\left(\boldsymbol{\chi}^{0,1}\right)\right| = 1; \tag{18}$$

the interfacial conditions on the sphere surface:

$$\mathbf{v}\cdot\mathbf{N} = 0; \qquad \mathbf{v} = \overline{\mathbf{v}}; \qquad \overline{\boldsymbol{\sigma}}\cdot\mathbf{N} = Ca_\mathrm{e}\boldsymbol{\sigma}\cdot\mathbf{N} \ \text{ at } \ r = 1 + \Delta, \tag{19}$$

and conditions that neither l nor $\mathbf{h}$ diverges as $r \to 0$.

Three new dimensionless parameters have emerged: the material fluid ratio ϵ, which is a property of the second-order fluid:

$$\epsilon = \frac{\alpha_0}{\alpha_1}, \tag{20}$$

Wi, the Weissenberg number, the ratio of elastic to viscous forces in the fluid phase:

$$Wi = \frac{\alpha_1 ||\mathbf{E}^\infty||}{\eta_0}, \tag{21}$$

and the elastic capillary number Ca_e, defined as

$$Ca_\mathrm{e} = \frac{\eta_0 ||\mathbf{E}^\infty||}{\mu} \tag{22}$$

which represents the relative magnitude of fluid stresses to solid stresses. The latter two will be treated as small parameters, whereas it is expected for homogeneous fluids that $\epsilon \leq -0.5$ (Ho and Leal, 1976, based on experimental observations).

2.5. Quantity expansions

We have two small parameters in our problem, the Weissenberg number $Wi \ll 1$ and the elastic capillary number $Ca_\mathrm{e} \ll 1$, and we express all our physical quantities as expansions in these parameters, in general keeping terms up to and including the first interaction between viscoelasticity of the fluid and deformation of the particle. We use the general expansion form for a quantity Y:

$$Y = Y^0 + Wi Y^{1Wi} + Ca_\mathrm{e} Y^{1Ca_\mathrm{e}} + Ca_\mathrm{e} Wi Y^{2CW} + O(Ca_\mathrm{e}^2, Wi^2) \tag{23}$$

The quantity Y is any of the solid phase quantities $\mathbf{h}$, l, $\overline{\mathbf{v}}$, $\mathbf{e}$ and $\overline{\boldsymbol{\sigma}}$ or the fluid phase quantities p, $\mathbf{v}$, $\mathbf{E}$, $\mathbf{A}$ and $\boldsymbol{\sigma}$. In these expansions we have neglected terms of order Wi^2, which capture second-order effects of viscoelasticity, and those of order Ca_e^2, which capture second-order deformation effects; however, in order to calculate the first effect of viscoelasticity on the particle shape, we will keep terms of order $Ca_\mathrm{e} Wi$. In the case of the second Rivlin–Ericksen tensor $\mathbf{A}$, because it appears with a prefactor of Wi in the governing equations, we will find that we can neglect the terms $\mathbf{A}^{1Wi}$ and $\mathbf{A}^{2CW}$.

The quantities Δ and $\hat{\mathbf{N}}$ are only defined at the interfacial boundary. Since viscoelasticity alone will not perturb the particle shape, they have the following expansions:

$$\begin{aligned} \Delta &= Ca_\mathrm{e} \rho^{1Ca_\mathrm{e}} + Ca_\mathrm{e} Wi\, \rho^{2CW} + O(Ca_\mathrm{e}^2, Ca_\mathrm{e} Wi^2), && (24) \\ \hat{N}_i &= \hat{N}_i^0 + Ca_\mathrm{e} \hat{N}_i^{1Ca_\mathrm{e}} + Ca_\mathrm{e} Wi\, \hat{N}_i^{2CW} + O(Ca_\mathrm{e}^2, Ca_\mathrm{e} Wi^2). && (25) \end{aligned}$$

Inserting these perturbation expansions into our governing equations and boundary conditions, and collecting terms of like order from each equation, we gather a complete set of equations and boundary conditions at each level of expansion. The governing equations in the fluid are:

$$\nabla_i v_i^0 = 0, \qquad \nabla_i v_i^{1Wi} = 0, \qquad \nabla_i v_i^{1Ca_e} = 0, \qquad \nabla_i v_i^{2CW} = 0, \tag{26}$$

$$\nabla_j \sigma_{ij}^0 = 0, \qquad \nabla_j \sigma_{ij}^{1Wi} = 0, \qquad \nabla_j \sigma_{ij}^{1Ca_e} = 0, \qquad \nabla_j \sigma_{ij}^{2CW} = 0. \tag{27}$$

$$\begin{aligned} \sigma_{ij}^0 &= -p^0\delta_{ij} + 2E_{ij}^0, \qquad\qquad \sigma_{ij}^{1Ca_e} = -p^{1Ca_e}\delta_{ij} + 2E_{ij}^{1Ca_e}, &(28)\\ \sigma_{ij}^{1Wi} &= -p^{1Wi}\delta_{ij} + 2E_{ij}^{1Wi} + \epsilon A_{ij}^0 + 4E_{ik}^0 E_{kj}^0, &(29)\\ \sigma_{ij}^{2CW} &= -p^{2CW}\delta_{ij} + 2E_{ij}^{2CW} + \epsilon A_{ij}^{1Ca_e} + 4E_{ik}^0 E_{kj}^{1Ca_e} + 4E_{ik}^{1Ca_e} E_{kj}^0. &(30) \end{aligned}$$

and in the solid phase,

$$\nabla_i \overline{v}_i^0 = 0, \qquad \nabla_i \overline{v}_i^{1Wi} = 0, \qquad \nabla_i \overline{v}_i^{1Ca_e} = 0, \qquad \nabla_i \overline{v}_i^{2CW} = 0, \tag{31}$$

$$\nabla_j \overline{\sigma}_{ij}^{1Ca_e} = 0, \qquad\qquad \nabla_j \overline{\sigma}_{ij}^{2CW} = 0, \tag{32}$$

$$\overline{\sigma}_{ij}^{1Ca_e} = -l^{1Ca_e}\delta_{ij} + 2e_{ij}^{1Ca_e}, \qquad \overline{\sigma}_{ij}^{2CW} = -l^{2CW}\delta_{ij} + 2e_{ij}^{2CW}, \tag{33}$$

$$\nabla_j \overline{v}_i^0 + \nabla_i \overline{v}_j^0 = 0, \qquad\qquad \nabla_j \overline{v}_i^{1Wi} + \nabla_i \overline{v}_j^{1Wi} = 0, \tag{34}$$

$$\frac{De_{ij}^{1Ca_e}}{Dt} + e_{il}^{1Ca_e}\left(\nabla_j \overline{v}_l^0\right) + \left(\nabla_i \overline{v}_l^0\right) e_{lj}^{1Ca_e} = \frac{1}{2}\left(\nabla_j \overline{v}_i^{1Ca_e} + \nabla_i \overline{v}_j^{1Ca_e}\right), \tag{35}$$

$$\begin{aligned} \frac{De_{ij}^{2CW}}{Dt} + e_{il}^{1Ca_e}\left(\nabla_j \overline{v}_l^{1Wi}\right) + e_{il}^{2CW}\left(\nabla_j \overline{v}_l^0\right) + \left(\nabla_i \overline{v}_l^{1Wi}\right) e_{lj}^{1Ca_e} + \left(\nabla_i \overline{v}_l^0\right) e_{lj}^{2CW} \\ = \frac{1}{2}\left(\nabla_j \overline{v}_i^{2CW} + \nabla_i \overline{v}_j^{2CW}\right). \end{aligned} \tag{36}$$

The boundary conditions at the outer boundary of the fluid cell are:

$$v_i^0 = bE_{ik}^\infty \hat{n}_k + b\,\Omega_{ik}^\infty \hat{n}_k, \qquad\qquad v_i^{1Wi} = v_i^{1Ca_e} = v_i^{2CW} = 0 \quad \text{at } r = b. \tag{37}$$

At the interface between the particle and the fluid, we use a Taylor expansion in small Δ to move all the conditions to $r = 1$. From the material interface condition, the shape perturbation ρ (as defined in equation (24)) becomes:

$$\rho^{1Ca_\mathrm{e}} = h_i^{1Ca_\mathrm{e}}\hat{n}_i, \qquad\qquad \rho^{2CW} = h_i^{2CW}\hat{n}_i, \tag{38}$$

and the unit normal:

$$\hat{N}_i^0 = \hat{n}_i, \quad \hat{N}_i^{1Ca_\mathrm{e}} = \frac{\partial \rho^{1Ca_\mathrm{e}}}{\partial \hat{n}_j}\hat{n}_i\hat{n}_j - \frac{\partial \rho^{1Ca_\mathrm{e}}}{\partial \hat{n}_i}, \quad \hat{N}_i^{2CW} = \frac{\partial \rho^{2CW}}{\partial \hat{n}_j}\hat{n}_i\hat{n}_j - \frac{\partial \rho^{2CW}}{\partial \hat{n}_i}. \tag{39}$$

This allows us to express the remaining interfacial conditions in terms of $\hat{\mathbf{n}}$: no penetration

$$\begin{gathered} v_i^0\hat{n}_i = v_i^{1Wi}\hat{n}_i = 0, \qquad \rho^{1Ca_\mathrm{e}}\frac{\partial v_i^0}{\partial r}\hat{n}_i + v_i^0\hat{N}_i^{1Ca_\mathrm{e}} + v_i^{1Ca_\mathrm{e}}\hat{n}_i = 0, \\ \rho^{2CW}\frac{\partial v_i^0}{\partial r}\hat{n}_i + \rho^{1Ca_\mathrm{e}}\frac{\partial v_i^{1Wi}}{\partial r}\hat{n}_i + v_i^0\hat{N}_i^{2CW} + v_i^{1Wi}\hat{N}_i^{1Ca_\mathrm{e}} + v_i^{2CW}\hat{n}_i = 0 \quad \text{at } r = 1, \end{gathered} \tag{40}$$

matching velocities (no slip):

$$\begin{gathered} \overline{v}_i^0 = v_i^0, \qquad \overline{v}_i^{1Wi} = v_i^{1Wi}, \qquad \rho^{1Ca_\mathrm{e}}\frac{\partial \overline{v}_i^0}{\partial r} + \overline{v}_i^{1Ca_\mathrm{e}} = \rho^{1Ca_\mathrm{e}}\frac{\partial v_i^0}{\partial r} + v_i^{1Ca_\mathrm{e}}, \\ \rho^{2CW}\frac{\partial \overline{v}_i^0}{\partial r} + \rho^{1Ca_\mathrm{e}}\frac{\partial \overline{v}_i^{1Wi}}{\partial r} + \overline{v}_i^{2CW} = \rho^{2CW}\frac{\partial v_i^0}{\partial r} + \rho^{1Ca_\mathrm{e}}\frac{\partial v_i^{1Wi}}{\partial r} + v_i^{2CW} \quad \text{at } r = 1, \end{gathered} \tag{41}$$

and the traction condition:

$$\overline{\sigma}_{ik}^{1Ca_\mathrm{e}}\hat{n}_k = \sigma_{ik}^0\hat{n}_k, \qquad \overline{\sigma}_{ik}^{2CW}\hat{n}_k = \sigma_{ik}^{1Wi}\hat{n}_k \quad \text{at } r = 1. \tag{42}$$

Finally, the conditions that both displacement and Lagrange pressure remain nonsingular at $r = 0$ can be trivially generalised to all terms within their respective perturbation expansions.

Equations (26–42) give us a closed system within a single cell, up to first effects in deformation and viscoelasticity.

2.6. Average stress

In order to calculate rheometric functions, we need the ensemble average of the stress tensor $\boldsymbol{\sigma}$ over the whole suspension: that is, the solid particles, the cellular fluid, and the unperturbed fluid which occupies the region between the cells. We denote the whole domain by V, the region within a single cell of radius b as V_b, and the region inside a particle as V_p. If there are N particles, we can deduce the solid volume fraction $\phi = NV_p/V$.

To calculate the average, it is essential to work in terms of the deviation of each quantity from its mean across the whole suspension to avoid volume integrals which are not uniformly convergent. We write

$$\mathbf{E} = \mathbf{E}^\infty + \mathbf{E}', \qquad \boldsymbol{\Omega} = \boldsymbol{\Omega}^\infty + \boldsymbol{\Omega}', \tag{43}$$

with $\mathbf{E}^\infty$, $\boldsymbol{\Omega}^\infty$ mean tensors across the entire suspension. We note that equation (43) describes the deviated quantity at any position within the suspension e.g. $\overline{\mathbf{E}}' = \overline{\mathbf{E}} - \mathbf{E}^\infty$. The technique is similar to that used by Koch and Subramanian (2006), though they worked in the limit $b \to \infty$ and by Sherwood (2006), who did not consider the fluid outside the cells, and also to our previous work with rigid particles (Escott and Wilson, 2020). Full details can be found in Escott (2021).

We introduce the notation $\widehat{X_{ij}} = X_{ij} - \frac{1}{3}X_{kk}\delta_{ij}$ for the deviatoric part of a tensor $\mathbf{X}$, and $\langle\cdot\rangle$ for the ensemble average. We consider the system in its three distinct components: the pure fluid outside the cells, the cellular fluid volumes, and the elastic particles; for each of these components we will express the local deviatoric stress in terms of the quantities in equation (43) above.

The calculations in the fluid volumes, though subtle, are well understood (Koch and Subramanian, 2006, Rallison, 2012, Escott and Wilson, 2020); only the contribution from the elastic solid is new in this work. Within the particles, we introduce an *extra particle stress* $\mathbf{P}$, the difference between the true stress and the stress we would see if the second-order fluid were present throughout:

$$P_{ij} = \sigma_{ij} - \left[-p\delta_{ij} + 2E_{ij} + Wi(\epsilon A_{ij} + 4E_{ik}E_{kj})\right]. \tag{44}$$

The term which has been removed can be incorporated into the calculation for the cellular fluid. The volume integral of P_{ij} over a single solid particle can, in turn, be split into the stresslet $\boldsymbol{\sigma}^S$ (which is in its standard form for rigid particles, though the boundary has deformed):

$$\sigma^S_{ij} = \frac{1}{2V^p} \int_{r=1+\Delta} r \, \widehat{\left(\sigma_{ik}\hat{n}_j + \sigma_{kj}\hat{n}_i\right)} \, \hat{N}_k \mathrm{d}S, \tag{45}$$

and the particle-induced fluid stress (PIFS) $\boldsymbol{\sigma}^P$ generated by a single particle:

$$\begin{aligned} \sigma^P_{ij} = -\frac{1}{V^p} \int_{r=1+\Delta} \left(\overline{v}_i \hat{N}_j + \overline{v}_j \hat{N}_i\right) \mathrm{d}S + \frac{4\epsilon Wi}{V^p} \int_{V^b - V^p} \widehat{E'_{ik}\Omega'_{kj}} \mathrm{d}V \\ + \frac{4\left(1+\epsilon\right)Wi}{V^p} \int_{V^b - V^p} \widehat{E'_{ik}E'_{kj}} \mathrm{d}V + \frac{4\epsilon Wi}{V^p} \int_{V^p} \widehat{\overline{E}'_{ik}\overline{\Omega}'_{kj}} \mathrm{d}V \\ + \frac{4\left(1+\epsilon\right)Wi}{V^p} \int_{V^p} \widehat{\overline{E}'_{ik}\overline{E}'_{kj}} \mathrm{d}V - \frac{4\epsilon Wi}{V^p} \int_{V^p} \widehat{\overline{E}_{ik}\overline{\Omega}_{kj}} \mathrm{d}V - \frac{4\left(1+\epsilon\right)Wi}{V^p} \int_{V^p} \widehat{\overline{E}_{ik}\overline{E}_{kj}} \mathrm{d}V, \end{aligned} \tag{46}$$

Using these insights, the ensemble average of the deviatoric bulk stress can be written as

$$\left\langle \widehat{\sigma_{ij}} \right\rangle_s = 2E^\infty_{ij} + Wi \left[4\epsilon \widehat{E^\infty_{ik}\Omega^\infty_{kj}} + 4\left(1+\epsilon\right) \widehat{E^\infty_{ik}E^\infty_{kj}}\right] + \phi \, \sigma^P_{ij} + \phi \, \sigma^S_{ij}. \tag{47}$$

We can then describe the full bulk stress as a perturbation series in our small parameters Wi and Ca_e:

$$\left\langle \widehat{\sigma_{ij}} \right\rangle_s = \left\langle \widehat{\sigma_{ij}} \right\rangle^0_s + Wi \left\langle \widehat{\sigma_{ij}} \right\rangle^{1Wi}_s + Ca_\mathrm{e} \left\langle \widehat{\sigma_{ij}} \right\rangle^{1Ca_\mathrm{e}}_s + O\left(Ca_\mathrm{e} Wi, Ca_\mathrm{e}^2, Wi^2\right) \tag{48}$$

in which

$$\left\langle \widehat{\sigma_{ij}} \right\rangle^0_s = 2E^\infty_{ij} - \frac{\phi}{V^p} \int_{r=1} \left(\overline{v}^0_i \hat{n}_j + \overline{v}^0_j \hat{n}_i\right) \mathrm{d}S + \frac{\phi}{2V^p} \int_{r=1} r \, \widehat{\left(\sigma^0_{ik}\hat{n}_j + \sigma^0_{kj}\hat{n}_i\right)} \, \hat{n}_k \mathrm{d}S, \tag{49}$$

$$\begin{aligned} \left\langle \widehat{\sigma_{ij}} \right\rangle^{1Wi}_s = 4\epsilon \widehat{E^\infty_{ik}\Omega^\infty_{kj}} + 4\left(1+\epsilon\right) \widehat{E^\infty_{ik}E^\infty_{kj}} - \frac{\phi}{V^p} \int_{r=1} \left(\overline{v}^{1Wi}_i \hat{n}_j + \overline{v}^{1Wi}_j \hat{n}_i\right) \mathrm{d}S \\ + \frac{4\epsilon\phi}{V^p} \int_{r=1}^{r=b} \widehat{E^0_{ik}{}' \Omega^0_{kj}{}'} \mathrm{d}V + \frac{4\left(1+\epsilon\right)\phi}{V^p} \int_{r=1}^{r=b} \widehat{E^0_{ik}{}' E^0_{kj}{}'} \mathrm{d}V \\ + \frac{4\epsilon\phi}{V^p} \int_{V^p} \widehat{\overline{E}^0_{ik}{}' \overline{\Omega}^0_{kj}{}'} \mathrm{d}V + \frac{4\left(1+\epsilon\right)\phi}{V^p} \int_{r=0}^{r=1} \widehat{\overline{E}^0_{ik}{}' \overline{E}^0_{kj}{}'} \mathrm{d}V - \frac{4\epsilon\phi}{V^p} \int_{r=0}^{r=1} \widehat{\overline{E}^0_{ik}\overline{\Omega}^0_{kj}} \mathrm{d}V \\ - \frac{4\left(1+\epsilon\right)\phi}{V^p} \int_{r=0}^{r=1} \widehat{\overline{E}^0_{ik}\overline{E}^0_{kj}} \mathrm{d}V + \frac{\phi}{2V^p} \int_{r=1} r \, \widehat{\left(\sigma^{1Wi}_{ik}\hat{n}_j + \sigma^{1Wi}_{kj}\hat{n}_i\right)} \, \hat{n}_k \mathrm{d}S, \end{aligned} \tag{50}$$

$$
\begin{aligned}
\langle\widehat{\sigma_{ij}}\rangle_s^{1Ca_\mathrm{e}} = &-\frac{\phi}{V^p}\int_{r=1}\left(\overline{v}_i^{1Ca_\mathrm{e}}\hat{n}_j + \overline{v}_i^0\hat{N}_j^{1Ca_\mathrm{e}} + \rho^{1Ca_\mathrm{e}}\frac{\partial\overline{v}_i^0}{\partial r}\hat{n}_j + 2\rho^{1Ca_\mathrm{e}}\overline{v}_i^0\hat{n}_j\right)\mathrm{d}S \\
&-\frac{\phi}{V^p}\int_{r=1}\left(\overline{v}_j^{1Ca_\mathrm{e}}\hat{n}_i + \overline{v}_j^0\hat{N}_i^{1Ca_\mathrm{e}} + \rho^{1Ca_\mathrm{e}}\frac{\partial\overline{v}_j^0}{\partial r}\hat{n}_i + 2\rho^{1Ca_\mathrm{e}}\overline{v}_j^0\hat{n}_i\right)\mathrm{d}S \\
&+\frac{\phi}{2V^p}\int_{r=1}\left(\sigma_{ik}^{1Ca_\mathrm{e}}\hat{n}_j\hat{n}_k + \sigma_{ik}^0\hat{n}_j\hat{N}_k^{1Ca_\mathrm{e}} \widehat{+ \rho^{1Ca_\mathrm{e}}}\frac{\partial\sigma_{ik}^0}{\partial r}\hat{n}_j\hat{n}_k + 3\rho^{1Ca_\mathrm{e}}\sigma_{ik}^0\hat{n}_j\hat{n}_k\right)\mathrm{d}S \\
&+\frac{\phi}{2V^p}\int_{r=1}\left(\sigma_{kj}^{1Ca_\mathrm{e}}\hat{n}_i\hat{n}_k + \sigma_{kj}^0\hat{n}_i\hat{N}_k^{1Ca_\mathrm{e}} \widehat{+ \rho^{1Ca_\mathrm{e}}}\frac{\partial\sigma_{kj}^0}{\partial r}\hat{n}_i\hat{n}_k + 3\rho^{1Ca_\mathrm{e}}\sigma_{kj}^0\hat{n}_i\hat{n}_k\right)\mathrm{d}S. \quad (51)
\end{aligned}
$$

2.7. Solution strategy

We will solve the governing equations at each order within a single cell and its particle, then use the ensemble average process from section 2.6 to produce viscometric functions for the suspension as a whole.

We begin with the leading-order flow, which corresponds to Newtonian flow around a rigid particle, then repeat the fluid calculation at $O(Wi)$ to capture the leading effects of viscoelasticity. The traction induced at the particle surface by the Newtonian fluid then informs the $O(Ca_\mathrm{e})$ deformation of the particle via the traction matching equation (42), and the viscoelastic perturbation will force deformation at order $Ca_\mathrm{e}Wi$. Finally, we calculate the effect of deformation on the fluid flow, giving contributions at order Ca_e and $Ca_\mathrm{e}Wi$ to the flow in the fluid phase. The limit $Ca_\mathrm{e} = 0$ is equivalent to (and validated against) our earlier work (Escott and Wilson, 2020), in which we considered rigid spheres suspended in a second-order fluid.

3. Results: Fluid flow

3.1. Newtonian solution

The leading-order flow solution in the cellular fluid outside the solid particle is, of course, identical to that calculated outside a truly rigid sphere in our earlier work (Escott and Wilson, 2020). However, our mathematical presentation here is slightly different to the previous case: we formulate in terms of the unit vector $\hat{\mathbf{n}}$ rather than the position vector $\mathbf{x} = r\hat{\mathbf{n}}$ for convenience in later sections when the particle surface deforms.

We note first that the interfacial conditions of equation (19) imply that $\overline{\boldsymbol{\sigma}}^0 = \mathbf{0}$ and therefore $l^0 = 0$ and $\mathbf{e}^0 = \mathbf{0}$, i.e. no deformation, as we expect. We are solving only for $\overline{\mathbf{v}}^0$ in the solid, and $\mathbf{v}^0$, $\boldsymbol{\sigma}^0$ and p^0 in the fluid. We exploit the linearity of Stokes flow (viscoelastic terms appearing at a higher order) and the spherical symmetry of the geometry to write down the most general possible velocity and pressure profiles:

$$\begin{aligned}
v_i^0 &= V_1^0\left(r\right) E_{ik}^{\infty}\hat{n}_k + V_2^0\left(r\right) E_{jk}^{\infty}\hat{n}_i\hat{n}_j\hat{n}_k + V_3^0\left(r\right)\Omega_{ik}^{\infty}\hat{n}_k,\\
p^0 &= P_1^0\left(r\right) E_{jk}^{\infty}\hat{n}_j\hat{n}_k,\\
\overline{v}_i^0 &= \overline{V}_1^0\left(r\right) E_{ik}^{\infty}\hat{n}_k + \overline{V}_2^0\left(r\right) E_{jk}^{\infty}\hat{n}_i\hat{n}_j\hat{n}_k + \overline{V}_3^0\left(r\right)\Omega_{ik}^{\infty}\hat{n}_k.
\end{aligned} \tag{52}$$

Each of our governing equations (26–27) and (36) produces an ordinary differential equation in r for these functions, whose solutions are:

$$\begin{aligned}
V_1^0\left(r\right) &= \frac{C_1^0}{r^4} + \frac{C_2^0}{r^2} + C_3^0 r + C_4^0 r^3 + \frac{C_7^0 r^3}{5} - \frac{C_8^0}{5r^2},\\
V_2^0\left(r\right) &= -\frac{5C_1^0}{2r^4} - \frac{5C_4^0 r^3}{2} + \frac{C_8^0}{2r^2}, \qquad\qquad V_3^0\left(r\right) = C_5^0 r + \frac{C_6^0}{r^2},
\end{aligned} \tag{53}$$

$$P_1^0\left(r\right) = C_7^0 r^2 + \frac{C_8^0}{r^3}, \tag{54}$$

$$\overline{V}_1^0\left(r\right) = 0, \qquad\qquad \overline{V}_2^0\left(r\right) = 0, \qquad\qquad \overline{V}_3^0\left(r\right) = \overline{C}_5^0 r. \tag{55}$$

The constants C_i^0 and $\overline{C}_5^0$ are determined by applying the boundary conditions, and have the following form:

$$\begin{aligned}
C_1^0 &= \frac{-4b^5\left(1+b+b^2+b^3+b^4\right)}{\left(b-1\right)^3\left(4+16b+40b^2+55b^3+40b^4+16b^5+4b^6\right)},\\
C_2^0 &= \frac{-4b^3\left(1+b+b^2+b^3+b^4+b^5+b^6\right)}{\left(b-1\right)^3\left(4+16b+40b^2+55b^3+40b^4+16b^5+4b^6\right)},\\
C_3^0 &= (21/4)C_1^0 - (25/4)C_2^0, \qquad C_4^0 = C_2^0 - C_1^0,\\
C_5^0 &= \overline{C}_5^0 = 1, \qquad C_6^0 = 0, \qquad C_7^0 = (105/4)(C_2^0 - C_1^0), \qquad C_8^0 = 5C_2^0.
\end{aligned} \tag{56}$$

In fact, not all of these constants are determined by leading-order boundary conditions: it is the $O(Ca_{\mathrm{e}})$ term of the traction matching condition (42) that fixes $C_5^0 = 1$.

Given an imposed flow specified by $\mathbf{E}^\infty$ and $\mathbf{\Omega}^\infty$, these functions can be used to deduce the velocity at all points in the fluid and solid regions. In figure 2 we illustrate this for the case $b = 3$ for an xy-shear flow. We can see the rigid body rotation of the solid sphere and a fluid flow which is identical to that seen in earlier studies using the cell model with Newtonian fluids and rigid particles (e.g. Escott and Wilson, 2020).

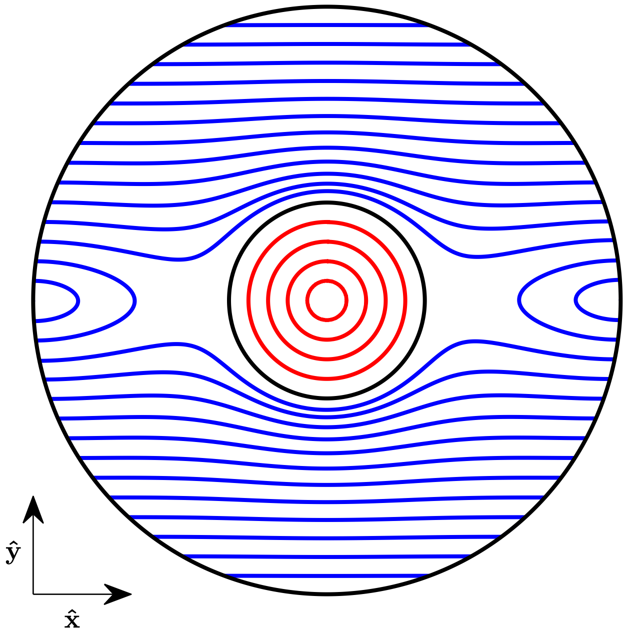

Figure 2: The velocity plot within one cell at leading order (i.e. neglecting effects of elasticity in both the solid and fluid phases). An xy shear flow is imposed at the cell boundary, which is located a distance $b = 3$ from the origin.

3.2. First effects of viscoelasticity

At this order of approximation, there is no deformation to the solid particle. We solve for the fluid pressure p, and velocity $\mathbf{v}$ and the solid velocity $\overline{\mathbf{v}}$. The second-order fluid introduces terms of quadratic order in the velocity gradient tensor $\mathbf{L}$ (and hence of the boundary forcings $\mathbf{E}^\infty$ and $\mathbf{\Omega}^\infty$), but there is still no distinguished direction other than $\hat{\mathbf{n}}$ so we can write the most general possible solution for each of our quantities in terms of the distance r from the particle centre as:

$$\begin{aligned} v_i^{1Wi} &= V_1^{1Wi}(r)\, E_{jk}^\infty E_{lm}^\infty \hat{n}_i\hat{n}_j\hat{n}_k\hat{n}_l\hat{n}_m + V_2^{1Wi}(r)\, E_{jk}^\infty E_{kl}^\infty \hat{n}_i\hat{n}_j\hat{n}_l + V_3^{1Wi}(r)\, E_{jk}^\infty E_{jk}^\infty \hat{n}_i \\ &\quad + V_4^{1Wi}(r)\, E_{il}^\infty E_{jk}^\infty \hat{n}_j\hat{n}_k\hat{n}_l + V_5^{1Wi}(r)\, E_{ik}^\infty E_{kl}^\infty \hat{n}_l + V_6^{1Wi}(r)\, E_{jk}^\infty \Omega_{kl}^\infty \hat{n}_i\hat{n}_j\hat{n}_l \\ &\quad + V_7^{1Wi}(r)\, E_{jk}^\infty \Omega_{il}^\infty \hat{n}_j\hat{n}_k\hat{n}_l + V_8^{1Wi}(r)\, E_{ik}^\infty \Omega_{kl}^\infty \hat{n}_l + V_9^{1Wi}(r)\, E_{kl}^\infty \Omega_{ik}^\infty \hat{n}_l, \\ p^{1Wi} &= P_1^{1Wi}(r)\, E_{jk}^\infty E_{lm}^\infty \hat{n}_j\hat{n}_k\hat{n}_l\hat{n}_m + P_2^{1Wi}(r)\, E_{jk}^\infty E_{kl}^\infty \hat{n}_j\hat{n}_l + P_3^{1Wi}(r)\, E_{jk}^\infty E_{jk}^\infty, \end{aligned} \tag{57}$$

with an exactly analogous equation for $\overline{\mathbf{v}}^{1Wi}$. We have omitted terms in $\boldsymbol{\Omega}^\infty\boldsymbol{\Omega}^\infty$ for clarity, as there are no forcing terms or boundary conditions which involve these contributions, leading to a trivially zero scalar function. In the solid phase, of course, at this order we have $\overline{V}_n^{1Wi}(r) = 0$ (by calculation rather than by assumption) as in the limit of zero deformability $Ca_\mathrm{e} = 0$ the sphere cannot deform, and instead rotates as a rigid body.

As in section 3.1, each of our governing equations results in a set of coupled linear differential equations in the scalar functions $V_n^{1Wi}(r)$, $\overline{V}_n^{1Wi}(r)$ and $P_m^{1Wi}(r)$, where $1 \leq n \leq 9$ and $1 \leq m \leq 3$. We will not give these equations explicitly here, noting only that they incorporate forcing terms from the leading-order solution; a summary of the equations and their solutions is given in Appendix A and complete details are available in Escott (2021).

An example of the $O(Wi)$ velocity profile is shown in figure 3: as for the Newtonian order, this is exactly the same as seen in our earlier work (Escott and Wilson, 2020) in which the particle could not deform. We can see that there is no perturbation at this order to the solid velocity, and that the fluid velocity perturbation has the reflectional symmetry associated with quadratic terms in $\mathbf{E}^\infty$ and $\boldsymbol{\Omega}^\infty$.

3.3. First effects of deformation

At order Ca_e we see the first modifications to the solid displacement, velocity and Lagrange pressure as well as a perturbation velocity and pressure in the fluid as a result of the particle deformation.

The fluid phase obeys the Stokes flow equations at this order, just as in section 3.1, but with modifications to the boundary conditions. At the outer boundary, because we are now

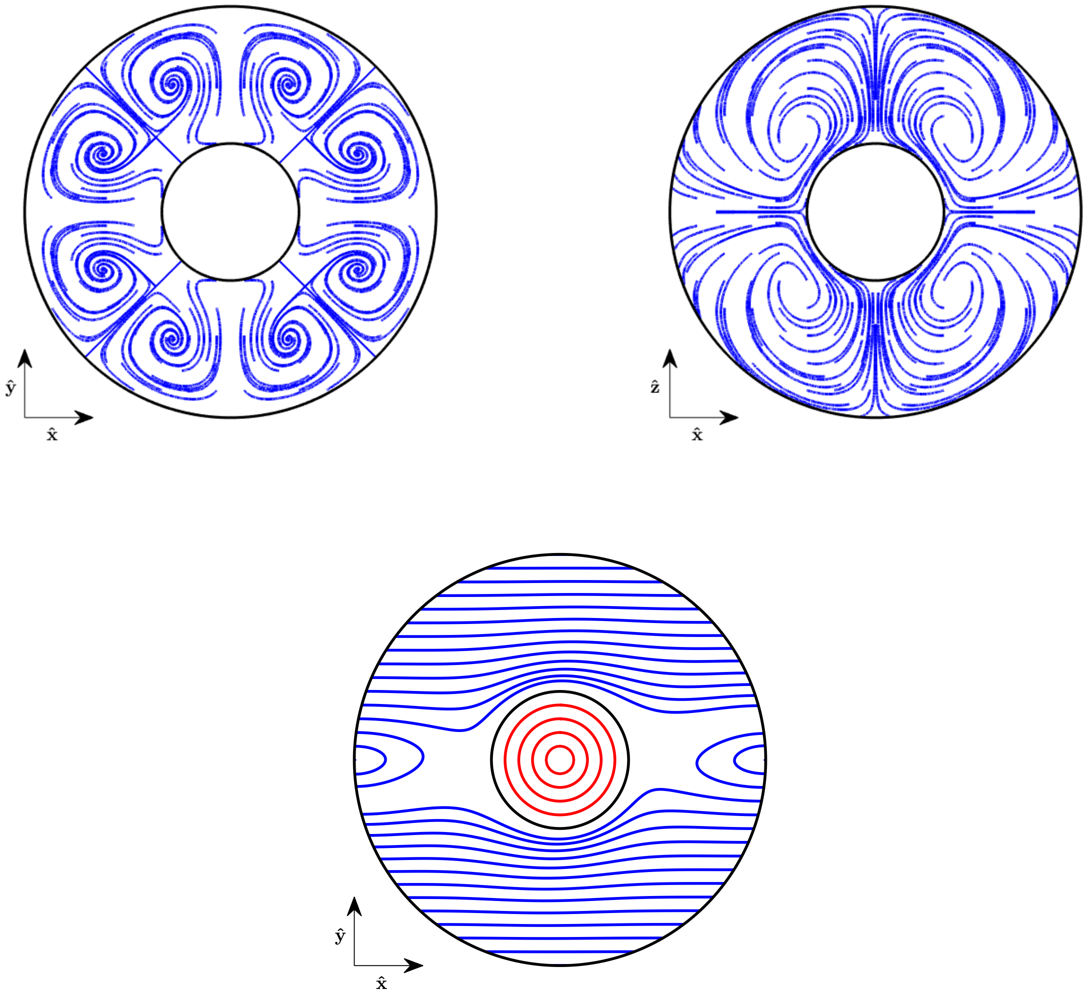

Figure 3: Velocity field at order Wi with $Ca_{\mathrm{e}} = 0$ in an xy-shear flow, taking $\epsilon = -8/14$ in the second-order fluid model. Top: fluid velocity $\mathbf{v}^{1Wi}$ in the xy-plane (left) and the xz-plane (right). Note the symmetry of these flow perturbations: this comes from the quadratic nature of their dependence on the background flow. Bottom: schematic of total fluid velocity $\mathbf{v}^0 + Wi\mathbf{v}^{1Wi}$ in the xy-plane, produced using an artificially large $Wi = 10$ to make the perturbation to the velocity visible.

solving for a perturbation to the Newtonian flow, the extra velocity $\mathbf{v}^{1Ca_{\mathrm{e}}}$ must be zero; but more significant are the extra driving terms at the particle surface.

The traction matching condition (42) uses $\boldsymbol{\sigma}^0$ which is linear in the background data $\mathbf{E}^\infty$ and $\boldsymbol{\Omega}^\infty$: we can deduce that $\overline{\boldsymbol{\sigma}}^{1Ca_{\mathrm{e}}}$ must also be linear in the background data, as must $\mathbf{e}^{1Ca_{\mathrm{e}}}$ and $l^{1Ca_{\mathrm{e}}}$. Similar arguments based on equations (36) and (41) allow us to deduce that $\overline{\mathbf{v}}^{1Ca_{\mathrm{e}}}$ and $\mathbf{v}^{1Ca_{\mathrm{e}}}$ must be quadratic in the background data; as in section 3.1 we discard terms in $\boldsymbol{\Omega}^\infty \cdot \boldsymbol{\Omega}^\infty$ (we calculated these explicitly and they are all zero).

Although there are two unit vectors available for our tensor descriptions, the radial vector $\hat{\mathbf{n}}$ and the particle unit normal $\hat{\mathbf{N}}$, these differ by order Ca_{e} so we can proceed at this order using $\hat{\mathbf{n}}$ as before. We produce the general forms:

$$\begin{aligned}
v_i^{1Ca_{\mathrm{e}}} &= V_1^{1Ca_{\mathrm{e}}}(r)\, E^\infty_{jk}E^\infty_{lm}\hat{n}_i\hat{n}_j\hat{n}_k\hat{n}_l\hat{n}_m + V_2^{1Ca_{\mathrm{e}}}(r)\, E^\infty_{jk}E^\infty_{kl}\hat{n}_i\hat{n}_j\hat{n}_l \\
&\quad + V_3^{1Ca_{\mathrm{e}}}(r)\, E^\infty_{jk}E^\infty_{jk}\hat{n}_i + V_4^{1Ca_{\mathrm{e}}}(r)\, E^\infty_{il}E^\infty_{jk}\hat{n}_j\hat{n}_k\hat{n}_l + V_5^{1Ca_{\mathrm{e}}}(r)\, E^\infty_{ik}E^\infty_{kl}\hat{n}_l \\
&\quad + V_6^{1Ca_{\mathrm{e}}}(r)\, E^\infty_{jk}\Omega^\infty_{kl}\hat{n}_i\hat{n}_j\hat{n}_l + V_7^{1Ca_{\mathrm{e}}}(r)\, E^\infty_{jk}\Omega^\infty_{il}\hat{n}_j\hat{n}_k\hat{n}_l \\
&\quad + V_8^{1Ca_{\mathrm{e}}}(r)\, E^\infty_{ik}\Omega^\infty_{kl}\hat{n}_l + V_9^{1Ca_{\mathrm{e}}}(r)\, E^\infty_{kl}\Omega^\infty_{ik}\hat{n}_l, \qquad (58) \\
p^{1Ca_{\mathrm{e}}} &= P_1^{1Ca_{\mathrm{e}}}(r)\, E^\infty_{jk}E^\infty_{lm}\hat{n}_j\hat{n}_k\hat{n}_l\hat{n}_m + P_2^{1Ca_{\mathrm{e}}}(r)\, E^\infty_{jk}E^\infty_{kl}\hat{n}_j\hat{n}_l \\
&\quad + P_3^{1Ca_{\mathrm{e}}}(r)\, E^\infty_{jk}E^\infty_{jk} + P_4^{1Ca_{\mathrm{e}}}(r)\, E^\infty_{jk}\Omega^\infty_{kl}\hat{n}_j\hat{n}_l, \qquad (59) \\
h_i^{1Ca_{\mathrm{e}}} &= H_1^{1Ca_{\mathrm{e}}}(r)\, E^\infty_{ik}\hat{n}_k + H_2^{1Ca_{\mathrm{e}}}(r)\, E^\infty_{jk}\hat{n}_i\hat{n}_j\hat{n}_k + H_3^{1Ca_{\mathrm{e}}}(r)\, \Omega^\infty_{ik}\hat{n}_k, \qquad (60) \\
l^{1Ca_{\mathrm{e}}} &= L_1^{1Ca_{\mathrm{e}}}(r)\, E^\infty_{jk}\hat{n}_j\hat{n}_k \qquad (61)
\end{aligned}$$

and an equation for $\overline{\mathbf{v}}^{1Ca_{\mathrm{e}}}$ which is identical to that for $\mathbf{v}^{1Ca_{\mathrm{e}}}$ except for the replacement of $V_n^{1Ca_{\mathrm{e}}}$ with $\overline{V}_n^{1Ca_{\mathrm{e}}}$ in each case. We also have the particle shape function and, from (39), the unit normal (these exist only at the surface so have no radial dependence):

$$\rho^{1Ca_{\mathrm{e}}} = \rho_1^{1Ca_{\mathrm{e}}} E^\infty_{jk}\hat{n}_j\hat{n}_k, \qquad \hat{N}_i^{1Ca_{\mathrm{e}}} = -2\rho_1^{1Ca_{\mathrm{e}}} E^\infty_{ik}\hat{n}_k + 2\rho_1^{1Ca_{\mathrm{e}}} E^\infty_{jk}\hat{n}_i\hat{n}_j\hat{n}_k. \qquad (62)$$

As in section 3.2, we do not give full details of the solutions here, as they are unwieldy; they are relegated to the appendix. We solve a set of linear differential equations for the

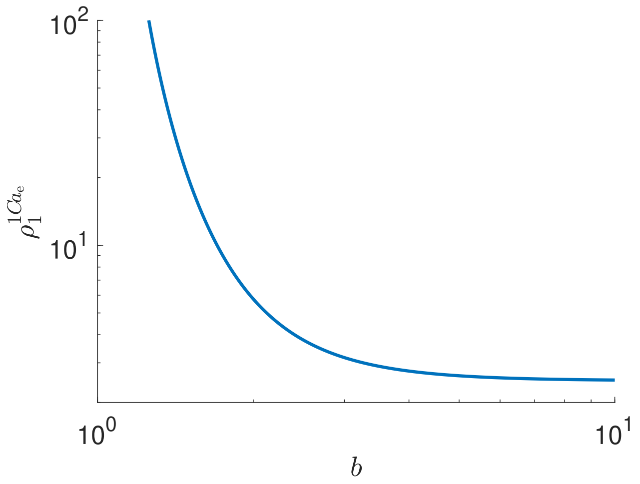

Figure 4: Log-log plot of the shape coefficient $\rho_1^{1Ca_\mathrm{e}}$ from equation (63) against cell radius b.

variables $V_n^{1Ca_\mathrm{e}}(r)$, $\overline{V}_n^{1Ca_\mathrm{e}}(r)$, $P_n^{1Ca_\mathrm{e}}$, $H_n^{1Ca_\mathrm{e}}$ and $L_1^{1Ca_\mathrm{e}}$, with boundary conditions which contain forcing from the leading-order case.

The explicit solutions for the solid deformation, velocity and Lagrange pressure and the fluid velocity at this order are given in section Appendix B; the shape function, however, is worth giving explicitly:

$$\rho_1^{1Ca_\mathrm{e}} = \frac{5}{68}\left(231C_1^0 - 265C_2^0\right) = \frac{5b^3\left(265 + 265b + 34b^2 + 34b^3 + 34b^4 + 34b^5 + 34b^6\right)}{17(b-1)^3\left(4 + 16b + 40b^2 + 55b^3 + 40b^4 + 16b^5 + 4b^6\right)}. \tag{63}$$

This shape function $\rho_1^{1Ca_\mathrm{e}}$ is plotted against b in figure 4. As expected, the deformation diverges in the limit of a very thin fluid layer $b \to 1$, and decreases monotonically up to the limit of an infinite cell $b \to \infty$; in that limit $\rho_1^{1Ca_\mathrm{e}} = 5/2$.

We can see a typical deformed particle shape, along with the full velocity profile, both inside and outside the solid deformed sphere, in figure 5, plotted for a Newtonian fluid in a cell of size $b = 3$. The first three images give the perturbation velocity fields in the three planes of the flow; the fourth uses an illustrative value $Ca_\mathrm{e} = 0.1$ to show the total velocity in the plane of shear. We can see a clear tank-treading motion within the particle, which is similar to the case of fluid capsules surrounded by an incompressible membrane (Sui et al.,

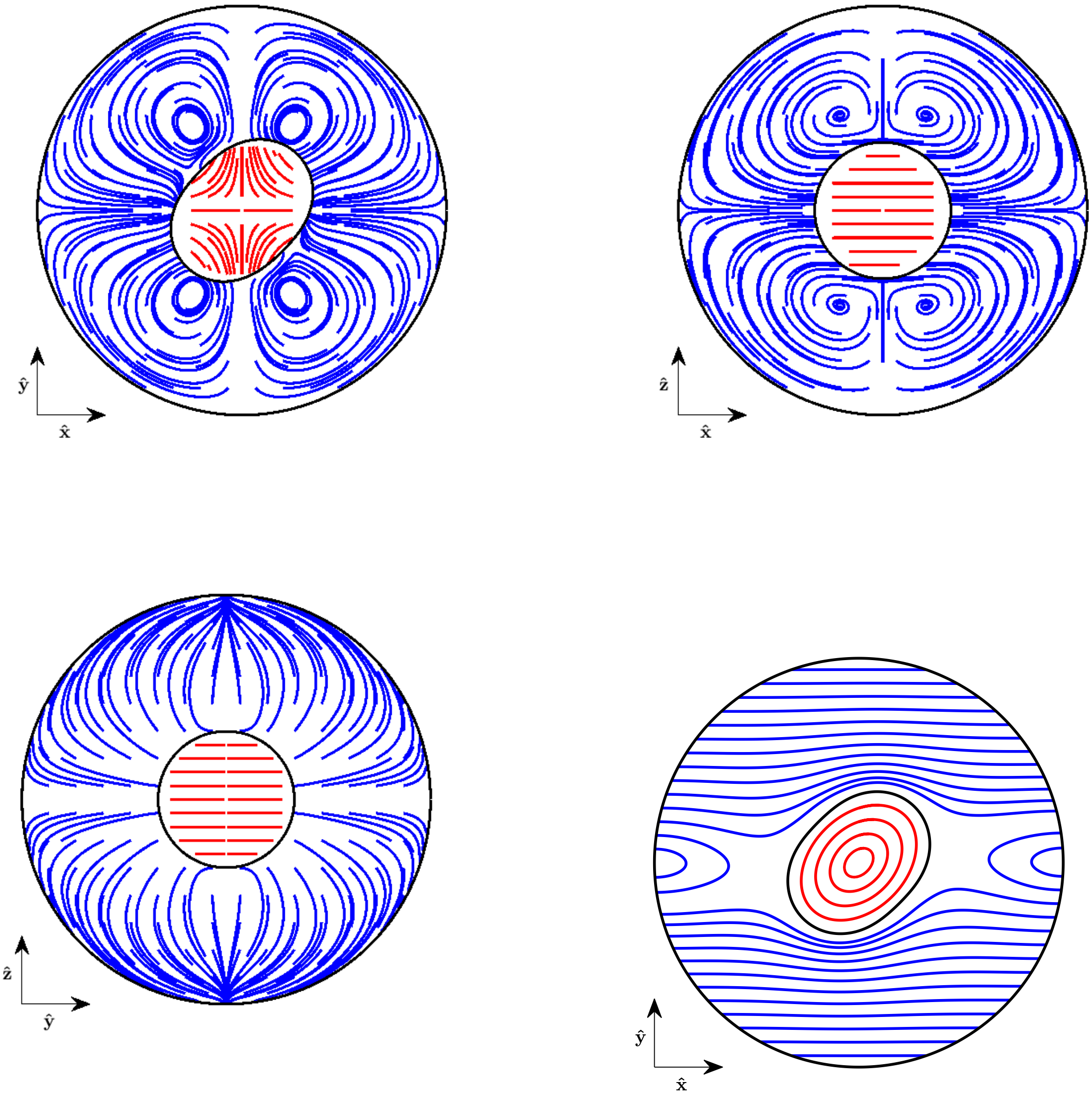

Figure 5: Velocities at order Ca_e in an xy-shear flow. Top left to bottom right: $\mathbf{v}^{1Ca_\mathrm{e}}$ in the xy, xz, yz-planes; total velocity $\mathbf{v} = \mathbf{v}^0 + Ca_\mathrm{e}\mathbf{v}^{1Ca_\mathrm{e}}$ for an illustrative value $Ca_\mathrm{e} = 0.1$. The cell radius is $b = 3$, and we can see the deformation of the particle in the xy-plane.

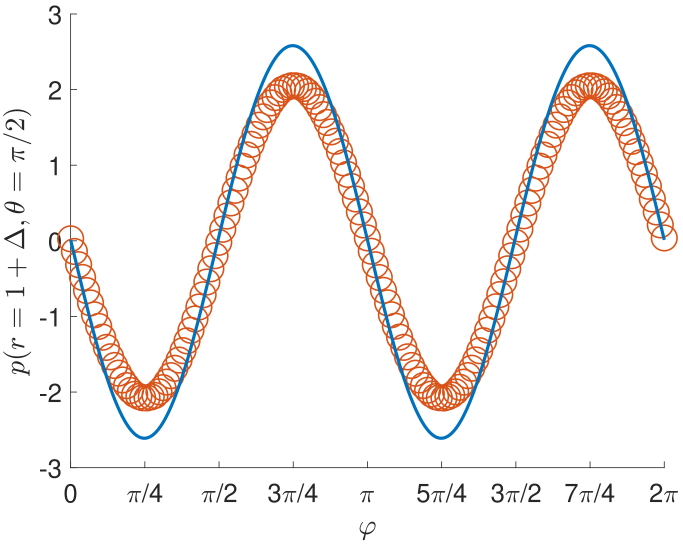

Figure 6: The pressure p on the particle surface (solid line), in xy shear flow, up to first effects of deformation in a Newtonian fluid, compared with simulations (Gao and Hu, 2009), the data points. Simulations are two-dimensional, compared with our results in the plane of shear (the equatorial plane $\theta = \pi/2$). Both works take $Ca_e = 0.004$; we calculate a cell radius $b = 5.4623$ to match the solid volume fraction and Gao and Hu (2009) have $Re = 0.125$. There is good qualitative agreement between the two.

2008), and a nonzero perturbation velocity field within the particle which modifies $\overline{\mathbf{v}}$ such that the velocity remains tangential to the particle surface. This perturbation velocity field is compressive in the flow direction, extensional in the flow gradient direction, and neutral in the vorticity direction. This pattern is continued into the fluid phase along those axes, but the perturbation fluid velocity is dominated by a set of four vortices in the plane of shear, with centre just off the particle surface and located at azimuthal angles $\varphi \approx \pi/3$, $2\pi/3$, $4\pi/3$ and $5\pi/3$.

In figure 6 we compare our pressure profile p on the particle surface in the plane of shear to results taken from Gao and Hu (2009). Their simulations are two-dimensional and have a nonzero Reynolds number of 0.125 so we do not expect a fully quantitative comparison; qualitatively, we can see the two profiles are very similar.

3.4. Interaction of viscoelasticity with deformation

We have already solved to order Wi and order Ca_e, and the solutions we have found capture the most important effects of viscoelasticity and deformation. In this section we will go one step further, only so far as is necessary to predict the effect of viscoelasticity on the shape of the deformed particle. The governing equations are given in section 2.5, and we are solving for terms with the superscript $2CW$. At this order there is a cubic dependence on the background tensors $\mathbf{E}^\infty$ and $\mathbf{\Omega}^\infty$ for the velocities $\mathbf{v}^{2CW}$, $\overline{\mathbf{v}}^{2CW}$ and fluid pressure p^{2CW}; the solid displacement $\mathbf{h}^{2CW}$ and Lagrange pressure l^{2CW}, and hence the surface deformation ρ^{2CW} all have a quadratic dependence on these background tensors. We could write down the explicit forms for all these functions, as we did for our previous expansions, in terms of our three standard ingredients: the background tensors; tensors constructed from the distinguished direction $\hat{\mathbf{n}}$; and scalar functions of radius. In this paper we will not present the details of the solution at this order; rather, we present only the details of the shape function:

$$\rho^{2CW} = \rho_1^{2CW} E^\infty_{jk} E^\infty_{lm} \left(\hat{n}_j \hat{n}_k \hat{n}_l \hat{n}_m - \frac{1}{15} \left(\delta_{jl}\delta_{km} + \delta_{jm}\delta_{kl} \right) \right) \\ + \rho_2^{2CW} E^\infty_{jk} E^\infty_{kl} \left(\hat{n}_j \hat{n}_l - \frac{1}{3}\delta_{jl} \right) + \rho_3^{2CW} E^\infty_{jk} \Omega^\infty_{kl} \left(\hat{n}_j \hat{n}_l - \frac{1}{3}\delta_{jl} \right). \quad (64)$$

in which the coefficients ρ_i^{2CW} depend on the two parameters b and ϵ. The explicit forms of ρ_1^{2CW} and ρ_2^{2CW} can be found in Escott (2021) and in the supplementary files (they are very unwieldy so we do not reproduce them here); however ρ_3^{2CW} relates directly to an earlier coefficient: $\rho_3^{2CW} = 2\epsilon\rho_1^{1Ca_\mathrm{e}}$.

We plot the coefficients of each term in the shape function ρ^{2CW} in figure 7. Each of these terms multiplies one of the spherical harmonics in equation (64) to produce the overall shape deformation.

There are strong similarities between the behaviours of ρ_1^{2CW} and ρ_3^{2CW}, though they differ in sign: there is only weak dependence on the viscoelastic constant ϵ, and an increase in magnitude with decreasing b. As $b \to \infty$ at constant ϵ, all three coefficients tend to finite

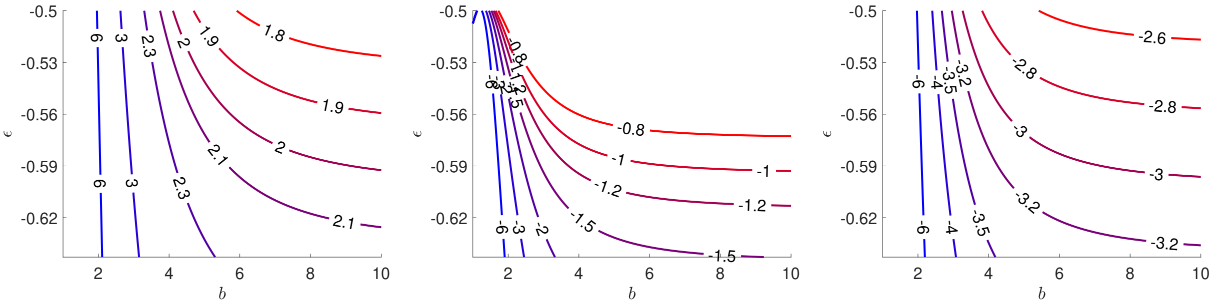

(a) ρ_1^{2CW} **(b)** ρ_2^{2CW} **(c)** ρ_3^{2CW}

Figure 7: Contour plots of the shape coefficients ρ_i^{2CW} in the b-ϵ plane. Note the non-monotonic behaviour of ρ_2^{2CW} for small b at $\epsilon \approx -1/2$.

constant values. Perhaps the most surprising behaviour is that of ρ_2^{2CW} for $b \to 1$, where the divergence for very thin fluid layers is dominated by a term proportional to $273 + 538\epsilon$, which changes sign at $\epsilon = -273/538 \approx -0.507$.

To complete this section on fluid flow, we compare our semi-analytical results for fluid velocity with simulation results from the literature. Work by Einarsson et al. (2017), Yang and Shaqfeh (2018a), and Guido and Shaqfeh (2019) has shown that, in shear flow, the polymer shear stress component exhibits localised regions of high stress close to the particle surface, which decrease within a short distance from the solid surface. In figure 8, we present our calculations alongside results from figure 11 of Guido and Shaqfeh (2019), using a Weissenberg number $Wi = 0.6288$ which exceeds the applicability of our asymptotic analysis but nonetheless gives an indication of the trends of our results. The quantity plotted here is the polymer shear stress as defined by Guido and Shaqfeh (2019), which equates to $\sigma_{xy} - \beta\sigma_{xy}^0$, where $\beta = 0.69$ is the ratio of solvent to total viscosity in the Giesekus model they use.

We can see that we reproduce qualitatively the four-lobed structure of the far-field stress distribution, though there are subtle differences in the angles of the lobes, with our principal far-field stress peak aligned more closely to the extensional axis than observed in the simulations. We also find, as in the simulations, that the stresses peak close to the particle surface. However, this is not the best graphic in which to see those near-field stresses, so

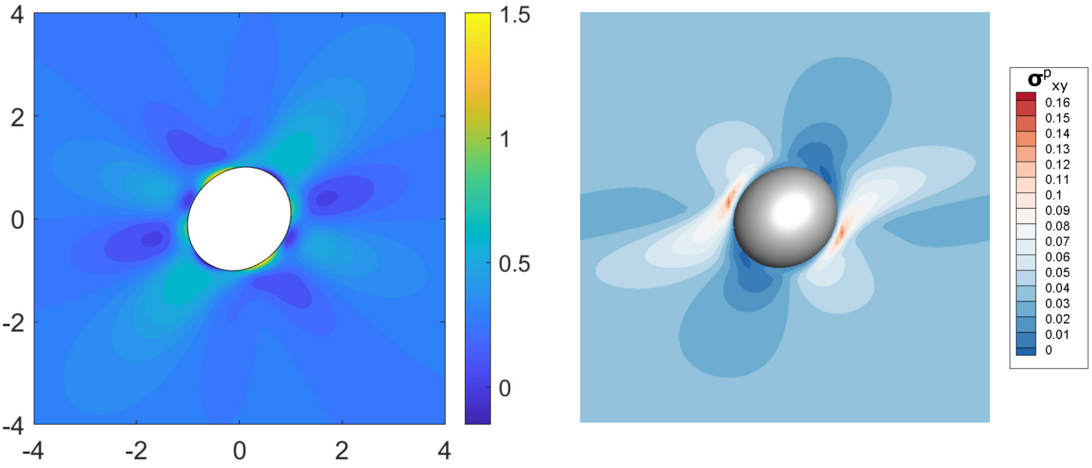

Figure 8: Comparison of shear stress with the literature in xy-shear flow. We plot polymer shear stress σ^p_{xy} as defined in Guido and Shaqfeh (2019), given $Ca_\mathrm{e} = 0.05$ and $Wi = 0.6288$. Left: our work with $b = 6.2035$. Right: figure 11b of Guido and Shaqfeh (2019): simulations of a Giesekus fluid with corresponding fluid parameters. Both images show a characteristic four-lobed shape, with a small region of high shear stress near the particle surface, just off the x-axis.

in figure 9 we present the shear stress value plotted against azimuthal angle φ around the particle, at the particle surface and two positions slightly beyond the surface.

Unlike the simulation results, we see that our stress peaks on the particle surface, not further out into the fluid; and while the near-field stress peak in both our work and simulations is close to the compressive axis $\varphi_c = 3\pi/4,\ 7\pi/4$, we see the peak displaced towards the flow gradient direction ($\varphi < \varphi_c$) while in simulations the peak is displaced towards the flow direction ($\varphi > \varphi_c$). These high values of the stress drop off rapidly as we move away from the fluid surface, as seen in the numerical simuations.

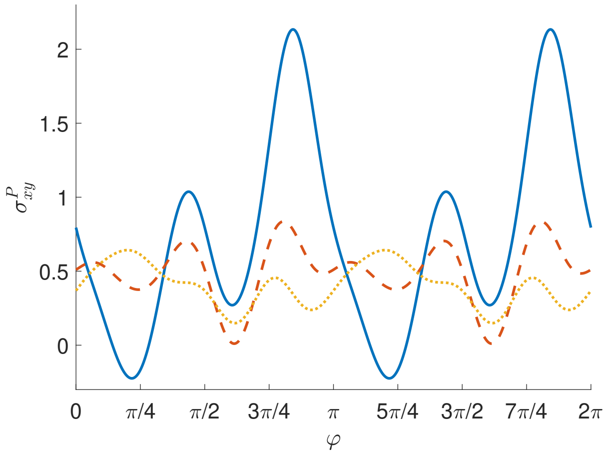

Figure 9: Polymer shear stress (as defined by Guido and Shaqfeh, 2019) on and close to the particle surface. We include terms up to order Wi and Ca_e. We show the results in the shear plane $z = 0$ as a function of the azimuthal angle φ, to accompany the results shown in Figure 8. The cell radius, elastic capillary number and Weissenberg number are $b = 6.2035$, $Ca_\mathrm{e} = 0.05$ and $Wi = 0.6288$ respectively. Solid blue line: particle surface; red dashed line: 1.1 × surface radius; yellow dotted line: 1.2 × surface radius.

4. Results: Particle deformation

4.1. Particle shape at $O(Ca_\mathrm{e})$

The largest change to the shape of the particle surface comes from the solution at order Ca_e, where it is given by the equation

$$r = 1 + Ca_\mathrm{e}\rho_1^{1Ca_\mathrm{e}} E_{jk}^{\infty}\hat{n}_j\hat{n}_k, \tag{65}$$

as solved in section 3.3, which is roughly ellipsoidal for small Ca_e. In the limit $b \to \infty$ this is in agreement with analytical work in the existing literature (Roscoe, 1967, Murata, 1981). Equation (65) is correct up to order Ca_e: as we include further terms in the expansion we will introduce higher harmonics to the shape function.

In figure 10 we plot the deformed particle shape for various values of the fluid cell radius b, at an illustrative value $Ca_\mathrm{e} = 0.1$, alongside the undeformed shape (which of course applies when $Ca_\mathrm{e} = 0$ regardless of b); then we show the same deformed particle shapes, but this time for a constant choice of cell radius $b = 3$, at different cross-sections in the xy-plane

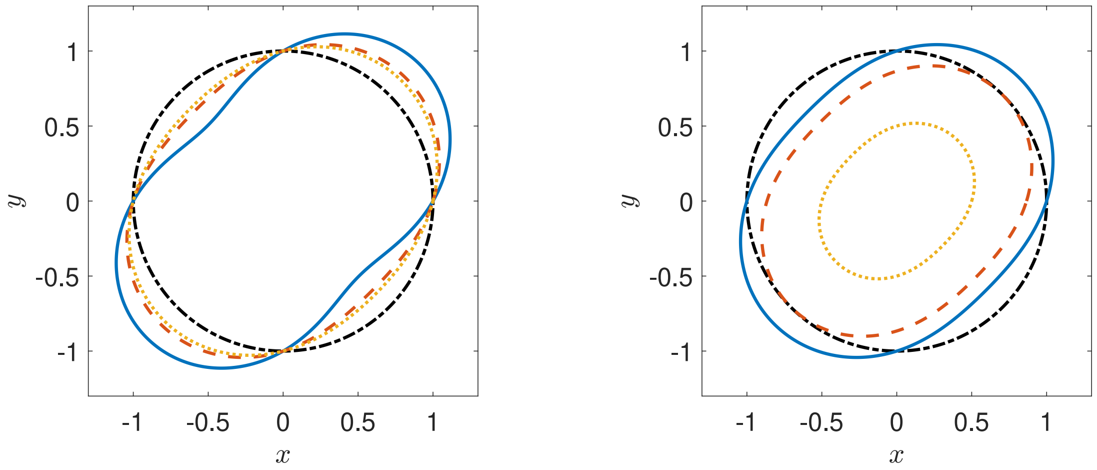

Figure 10: Shape of the deformed particle in simple xy shear flow, $\mathbf{v}^{\infty} = \dot{\gamma} y \hat{\boldsymbol{x}}$. The contour is shown in the shear plane with the extensional axis corresponding to an azimuthal angle $\varphi = \pi/4,\ 5\pi/4$. The deformation from a circular shape is small, but in this graphic is exaggerated with elastic capillary number $Ca_{\mathrm{e}} = 0.1$ for visibility. The dash-dotted line in both figures represents the undeformed $Ca_{\mathrm{e}} = 0$ radius.
Left: shape on the equator $\theta = \pi/2$. The solid, dashed and dotted lines represent $b = 2$, 3 and 10 respectively. Right: fixed $b = 3$. The solid, dashed and dotted lines represent cross-sections through the particle at $\theta = \pi/2$, $\pi/3$ and $\pi/6$ respectively.

(the boundary of the particle at fixed values of the polar angle θ). As one would expect, the small cross-sections close to the pole $\theta = 0$ are close to circular. We can see that the cell is extended (maximal radial deviation) in the extensional direction, as expected; and that as b decreases, the radial displacement increases in magnitude. The shapes in figure 10 are qualitatively similar to those found in Gao and Hu (2009), Villone et al. (2014) and Guido and Shaqfeh (2019) who each perform numerical analysis on a similar problem.

4.2. Quantifying deformation

A standard parameter to describe the degree of deformation of an ellipsoidal (or near-ellipsoidal) particle is the Taylor parameter T, defined as

$$T = \frac{L - B}{L + B} \tag{66}$$

with L and B the major and minor semi-axes respectively of our particle. In our formulation we have

$$T = \frac{Ca_\mathrm{e}\rho_1^{1Ca_\mathrm{e}}\left(\max\left[E_{jk}^\infty \hat{n}_j\hat{n}_k\right] - \min\left[E_{jk}^\infty \hat{n}_j\hat{n}_k\right]\right)}{2 + Ca_\mathrm{e}\rho_1^{1Ca_\mathrm{e}}\left(\max\left[E_{jk}^\infty \hat{n}_j\hat{n}_k\right] + \min\left[E_{jk}^\infty \hat{n}_j\hat{n}_k\right]\right)}, \tag{67}$$

and we recall here that in the dilute limit $b \to \infty$ we had $\rho_1^{1Ca_\mathrm{e}} \to 5/2$.

The quantity $E_{jk}^\infty \hat{n}_j\hat{n}_k$ is a second-order spherical harmonic which is maximised on the extensional axis of $\mathbf{E}^\infty$ and minimised on its compressive axis. For simple shear we have

$$L = 1 + \frac{1}{2}Ca_\mathrm{e}\rho_1^{1Ca_\mathrm{e}}, \qquad B = 1 - \frac{1}{2}Ca_\mathrm{e}\rho_1^{1Ca_\mathrm{e}}, \qquad T = \frac{1}{2}Ca_\mathrm{e}\rho_1^{1Ca_\mathrm{e}}, \tag{68}$$

and for pure uniaxial extension, the larger deformation

$$T = \frac{3Ca_\mathrm{e}\rho_1^{1Ca_\mathrm{e}}}{4 + Ca_\mathrm{e}\rho_1^{1Ca_\mathrm{e}}} = \frac{3}{4}Ca_\mathrm{e}\rho_1^{1Ca_\mathrm{e}} + O(Ca_\mathrm{e}^2). \tag{69}$$

In the dilute limit the latter expression gives $T = 15Ca_\mathrm{e}/8$, in agreement with Roscoe (1967), and we can also compare our values of the Taylor parameter T directly with numerical work from the literature. Villone et al. (2014) use simulations in shear flow, given a channel

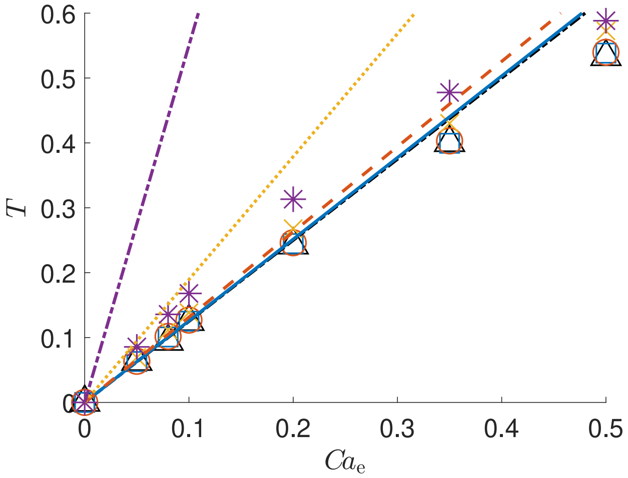

Figure 11: The Taylor parameter T, defined in equation (66), plotted against elastic capillary number for a variety of values of the confinement ratio $\beta = 1/b$. Lines are from the current work, points from the simulations of Villone et al. (2014). The lines and data points with increasing gradient represent $\beta = 0$, 0.1, 0.2, 0.4 and 0.6 respectively.

with infinite dimension in the vorticity direction, to investigate how the Taylor parameter might depend on the relative size of particle diameter and channel width, described by the *confinement ratio* β, defined as the ratio of particle diameter to channel width. In figure 11 we present a direct comparison with the current work, using the relation $\beta = 1/b$ for the confinement ratio (i.e. treating the cell size as the channel width). For small confinement $\beta \approx 0$ the results are very close, especially for low elastic capillary numbers – this is no surprise as this is the limit in which our analytical results are well validated against both analytical (Roscoe, 1967, Murata, 1981) and numerical work (Gao et al., 2012). There is deviation at larger values of Ca_{e}, as would be expected given that our expressions are valid only for small Ca_{e}; indeed, later in section 5.3 we argue that it is only sensible to consider values $Ca_{\mathrm{e}} \leq 0.1$. Finally there is substantial deviation as β increases, due to the fact that the nature of the confinement is very different in the two pieces of work.

4.3. Particle shape affected by viscoelasticity

In figure 12, we give an indicative view of the change in particle shape due to the interaction between deformation and fluid elasticity, using xy-shear as the illustrative flow. As we did at the previous order, we observe that deformation is more extreme for smaller values of the cell radius b; but in this case the peaks of deformation due to viscoelasticity are along the flow direction ($\varphi = 0$) rather than the extensional direction ($\varphi = \pi/4$).

4.4. Inclination angle (shear flow)

In shear flow, the *inclination angle* ζ is defined as the angle made between the major semi-axis and the flow direction. It is important because of the effect that the orientation of the particle has on the stresslet contribution to the first and second normal stress differences: it is observed (Villone et al., 2014, Guido and Shaqfeh, 2019) that these viscometric functions increase in magnitude when Wi increases, as a result of the principal axis of the particles beginning to align with the flow direction. This effect decreases at higher Wi, which is, of course, outside the scope of this work.

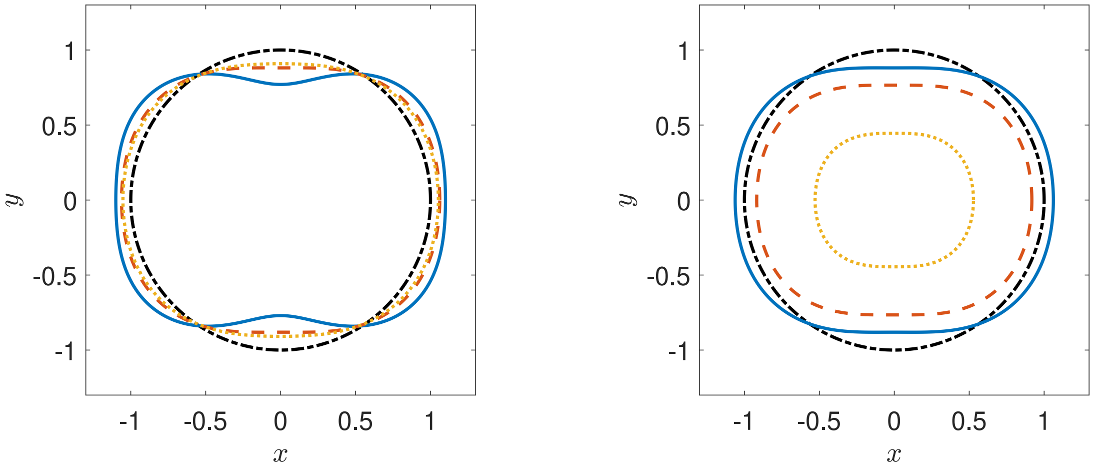

Figure 12: Particle deformation at order $Ca_\mathrm{e}Wi$, i.e. the sum of the second harmonic terms in equation (64). The parameter $\epsilon = -8/14$ throughout. We have fixed an unphysically large value $Ca_\mathrm{e}Wi = 0.1$ to allow the small deviations to be easily seen. The dash-dotted line in both figures represents the undeformed $Ca_\mathrm{e} = 0$ radius.
Left: effect of cell radius b in the plane of shear. The solid, dashed and dotted lines represent $b = 2$, 3 and 10 respectively. Right: fixed $b = 3$, cross-sections parallel to the plane of shear. The solid, dashed and dotted lines represent $\theta = \pi/2$, $\pi/3$ and $\pi/6$ respectively.

It is well known (e.g. Roscoe, 1967, Gao and Hu, 2009, Villone et al., 2014, and others) that the leading terms in small elastic capillary number are

$$\zeta = \frac{\pi}{4} - \frac{3Ca_\mathrm{e}}{4}. \tag{70}$$

From our calculation at order Ca_e we have the particle extended directly along the extensional axis, i.e. $\zeta = \pi/4$; the correction term comes from the solution for fluid flow at order Ca_e^2 which we have not included in this work since it is already well known. However, we will be able to calculate a correction due to the presence of viscoelasticity.

In order to calculate the angular position of the major semi-axis in a general linear flow, we start from the deformed radius, given in terms of the unit radial vector $\hat{\mathbf{n}}$ by combining equations (62) and (64) as

$$r = 1 + \mathit{Ca}_\mathrm{e}\rho_1^{1\mathit{Ca}_\mathrm{e}} E^\infty_{jk}\hat{n}_j\hat{n}_k + \mathit{Ca}_\mathrm{e}\mathit{Wi}\left\{\rho_1^{2\mathit{CW}} E^\infty_{jk}E^\infty_{lm}\left(\hat{n}_j\hat{n}_k\hat{n}_l\hat{n}_m - \frac{1}{15}\left(\delta_{jl}\delta_{km}+\delta_{jm}\delta_{kl}\right)\right)\right.$$
$$\left. + \rho_2^{2\mathit{CW}} E^\infty_{jk}E^\infty_{kl}\left(\hat{n}_j\hat{n}_l - \frac{1}{3}\delta_{jl}\right) + \rho_3^{2\mathit{CW}} E^\infty_{jk}\Omega^\infty_{kl}\left(\hat{n}_j\hat{n}_l - \frac{1}{3}\delta_{jl}\right)\right\}. \quad (71)$$

We can calculate the gradient of this function; in spherical polar coordinates, it will have zero radial component. By insisting that the other two components are also zero, we find two simultaneous equations which, when satisfied, define the position of a maximum or minimum in the radius function. The gradient is

$$\nabla_i r = \frac{\left(\delta_{ij} - \hat{n}_i\hat{n}_j\right)\mathit{Ca}_\mathrm{e}}{r}\left\{2E^\infty_{jk}\hat{n}_k\left(\rho_1^{1\mathit{Ca}_\mathrm{e}} + 2\mathit{Wi}\,\rho_1^{2\mathit{CW}}E^\infty_{lm}\hat{n}_l\hat{n}_m\right)\right.$$
$$\left. + 2\mathit{Wi}\,\rho_2^{2\mathit{CW}}E^\infty_{jk}E^\infty_{kl}\hat{n}_l + \mathit{Wi}\,\rho_3^{2\mathit{CW}}\left(E^\infty_{jk}\Omega^\infty_{kl} - \Omega^\infty_{jk}E^\infty_{kl}\right)\hat{n}_l\right\}, \quad (72)$$

so we require

$$2\left(\delta_{ij} - \hat{n}_i\hat{n}_j\right)E^\infty_{jk}\hat{n}_k\left(\rho_1^{1\mathit{Ca}_\mathrm{e}} + 2\mathit{Wi}\,\rho_1^{2\mathit{CW}}E^\infty_{lm}\hat{n}_l\hat{n}_m\right)$$
$$+ 2\left(\delta_{ij} - \hat{n}_i\hat{n}_j\right)\mathit{Wi}\,\rho_2^{2\mathit{CW}}E^\infty_{jk}E^\infty_{kl}\hat{n}_l + \left(\delta_{ij} - \hat{n}_i\hat{n}_j\right)\mathit{Wi}\,\rho_3^{2\mathit{CW}}\left(E^\infty_{jk}\Omega^\infty_{kl} - \Omega^\infty_{jk}E^\infty_{kl}\right)\hat{n}_l = 0. \quad (73)$$

Expanding the required angles as an asymptotic series in small Wi, we can calculate the leading-order and first correction terms to the angular position of the major semi-axis. For the special case of simple xy-shear, for which $\mathbf{E}^\infty = (\hat{\mathbf{x}}\hat{\mathbf{y}} + \hat{\mathbf{y}}\hat{\mathbf{x}})/2$, if we write $\hat{\mathbf{n}} = (\sin\theta\cos\varphi, \sin\theta\sin\varphi, \cos\theta))$, we have

$$r = 1 + \mathit{Ca}_\mathrm{e}\rho_1^{1\mathit{Ca}_\mathrm{e}}\sin^2\theta\sin\varphi\cos\varphi + \frac{1}{4}\mathit{Ca}_\mathrm{e}\mathit{Wi}\left(4\rho_1^{2\mathit{CW}}(\sin^4\theta\sin^2\varphi\cos^2\varphi - 1/15)\right.$$
$$\left. + \rho_2^{2\mathit{CW}}(\sin^2\theta - 2/3) - \rho_3^{2\mathit{CW}}\sin^2\theta(\cos^2\varphi - \sin^2\varphi)\right), \quad (74)$$

in which deformations are largest on the equator $\theta = \pi/2$. The inclination angle ζ can then be found by maximising this radius as a function of φ (fixing $\theta = \pi/2$); the first-order correction due to viscoelasticity (valid, of course, only for nonzero deformation $\mathit{Ca}_\mathrm{e} > 0$) is

$$\zeta = \frac{\pi}{4} + \frac{\mathit{Wi}}{4}\frac{\rho_3^{2\mathit{CW}}}{\rho_1^{1\mathit{Ca}_\mathrm{e}}} = \frac{\pi}{4} + \frac{\epsilon\mathit{Wi}}{2}. \quad (75)$$

since $\rho_3^{2CW} = 2\epsilon\rho_1^{1Ca_\mathrm{e}}$. Incorporating the result from equation (65) of Roscoe (1967), we can deduce that up to linear order in all elasticities, the inclination angle is given by

$$\zeta = \frac{\pi}{4} - \frac{3Ca_\mathrm{e}}{4} + \frac{\epsilon Wi}{2}. \tag{76}$$

Given that ϵ is negative (Ho and Leal, 1976), this means that weak viscoelasticity in the fluid acts to enhance the rotation of inclination angle caused by higher-order terms in the particle deformation. This agrees with the observations of analysis of Villone et al. (2014) and Guido and Shaqfeh (2019) that increasing Wi causes the particle to align more with the flow direction.

5. Results: Suspension rheology

5.1. Effective viscosity and relation between b and ϕ

Throughout our work we have had two distinct parameters: b, which governs the size of the fluid layer surrounding each particle, and ϕ, the solid volume fraction. If we were to treat the whole system as a spherical cell, we would represent the dilute limit by $b \to \infty$, $\phi \to 0$ in the relationship $b = \phi^{-1/3}$; but as soon as we introduce multiple particles or a different shape of fluid volume, this relationship is less clear (though we would expect $b \sim \phi^{-1/3}$ for dilute systems); and away from the dilute limit it is not obvious what volume of fluid should be allocated to each particle. Should the depth of the fluid layer match the mean-field nearest neighbour separation in a real suspension? Or half that value? And is there a good estimate of that separation available?

In this work we use empirical observations to motivate our choice of relation between the two variables. As we did for a different system in Escott and Wilson (2020), we set the relation $b(\phi)$ such that the effective viscosity in simple shear for a Newtonian fluid is a good match to experiments. We then assume that the relation is unchanged by the presence of viscoelasticity and deformation, to deduce suspension rheology for non-dilute viscoelastic suspensions.

We begin with the effective viscosity η_{eff} of our suspension, which comes from the bulk stress in equation (47). In the limit $Wi = Ca_{\text{e}} = 0$ this becomes

$$\langle\widehat{\sigma_{ij}}\rangle_s = 2\left[1 + \frac{10b^3\left(1+b+b^2+b^3+b^4+b^5+b^6\right)\phi}{(b-1)^3\left(4+16b+40b^2+55b^3+40b^4+16b^5+4b^6\right)}\right]E_{ij}^{\infty}, \tag{77}$$

as in our earlier work (Escott and Wilson, 2020). The resultant effective viscosity η_{eff} is

$$\frac{\eta_{\text{eff}}}{\eta_0} = 1 + \frac{10b^3\left(1+b+b^2+b^3+b^4+b^5+b^6\right)\phi}{(b-1)^3\left(4+16b+40b^2+55b^3+40b^4+16b^5+4b^6\right)}. \tag{78}$$

We then use the Krieger–Dougherty (KD) viscosity function:

$$\frac{\eta}{\eta_0} = \left(1 - \frac{\phi}{\phi_m}\right)^{-5\phi_m/2}, \tag{79}$$

an empirical formula which correctly reduces to the Einstein viscosity in the dilute limit and works well for rigid particles at all volume fractions. It uses the single parameter ϕ_m, the maximum packing fraction (established as 0.64 for disordered spheres). Matching this form with the effective viscosity of equation (78) establishes a relation $b(\phi)$ which remains applicable when the particles are very close to rigid. Explicitly, we solve for $b(\phi)$ which satisfies the relation

$$\frac{10b^3\left(1+b+b^2+b^3+b^4+b^5+b^6\right)\phi}{(b-1)^3\left(4+16b+40b^2+55b^3+40b^4+16b^5+4b^6\right)} = \left(1 - \frac{\phi}{\phi_m}\right)^{-5\phi_m/2} - 1. \tag{80}$$

The result is a function which diverges for small ϕ and tends to 1 as $\phi \to \infty$. It is plotted in figure 13 and tabulated in Escott and Wilson (2020).

While the KD viscosity function is based on rigid, not deformable, spheres, comparison with computational work by Guido and Shaqfeh (2019) shows that the intrinsic effective viscosity $\eta_{\text{eff}}' = \left(\eta_{\text{eff}} - \eta_0\right)/\eta_0\phi$ is within 1.6% of the KD value up to $Ca_{\text{e}} \approx 0.1$. This lends confidence in our results as long as we keep the parameter Ca_{e} small. We should note that the bulk stress does still depend on the deformation of the solid phase, even though there is no direct dependence through the viscosity matching: this dependence is entirely captured within the effective material functions, which occur at the first order of perturbation.

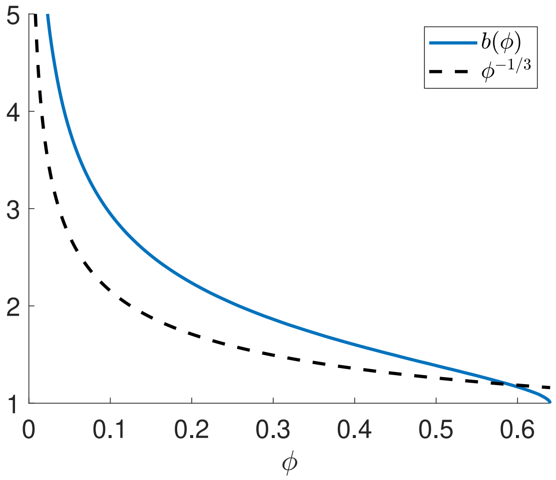

Figure 13: The relation $b(\phi)$ between cell radius and volume fraction, chosen to ensure the Krieger–Dougherty viscosity is fit correctly. Reproduced from Escott and Wilson (2020).

5.2. Effective material functions

Both our small parameters Wi and Ca_e are defined in terms of a material property and a flow rate: that is, for a given suspension if we change the flow rate both Wi and Ca_e will increase in tandem. However, their ratio is a property of the material itself, so we introduce the new dimensionless quantity

$$\Gamma = \frac{Wi}{Ca_\mathrm{e}} = \frac{\alpha_1 \mu}{{\eta_0}^2}, \tag{81}$$

also used by Guido and Shaqfeh (2019), which represents the strength of fluid elasticity relative to solid deformability. In theory, this can take all values in the range $[0, \infty)$ as we moved from deformable solids in a Newtonian fluid to rigid particles in a viscoelastic fluid, while keeping both Wi and Ca_e small (see section 5.3).

With the introduction of Γ, we can write the macroscopic stress, as given by equation (51), as:

$$\langle \widehat{\sigma_{ij}} \rangle_s = 2\frac{\eta_\mathrm{eff}}{\eta_0} E^\infty_{ij} + Wi \left(\Sigma_0 \widehat{E^\infty_{ik} \Omega^\infty_{kj}} + \Sigma_1 \widehat{E^\infty_{ik} E^\infty_{kj}} \right) \tag{82}$$

in which:

$$\begin{aligned}
\Sigma_0 &= 4\epsilon + \frac{\phi\,\Sigma_{0,1}}{\kappa\,(b-1)^3} + \Gamma^{-1}\frac{\phi\,\Sigma_{0,2}}{17\kappa^2\,(b-1)^6}, && (83)\\
\Sigma_1 &= 4\,(1+\epsilon) + \frac{\phi\,\Sigma_{1,1}}{7\kappa^3(b-1)^4} + \Gamma^{-1}\frac{\phi\,\Sigma_{1,2}}{119\kappa^3(b-1)^7} && (84)
\end{aligned}$$

and we have introduced the functions:

$$\begin{aligned}
\kappa &= 4 + 16b + 40b^2 + 55b^3 + 40b^4 + 16b^5 + 4b^6, && (85)\\
\Sigma_{0,1} &= 40b^3\left(1 + b + b^2 + b^3 + b^4 + b^5 + b^6\right)\epsilon, && (86)\\
\Sigma_{0,2} &= -200b^6\big(475 + 950b + 690b^2 + 430b^3 + 464b^4 + 498b^5 + 532b^6 + 351b^7\\
&\quad + 170b^8 + 136b^9 + 102b^{10} + 68b^{11} + 34b^{12}\big), && (87)\\
\Sigma_{1,1} &= 60b^3\big(-16\,(2+\epsilon) - 128b\,(2+\epsilon) - 576b^2\,(2+\epsilon) - 20b^3\,(157 + 66\epsilon)\\
&\quad - 160b^4\,(31 + 3\epsilon) + 8b^5\,(-417 + 724\epsilon) + 14b^6\,(343 + 1479\epsilon)\\
&\quad + 4b^7\,(4741 + 10718\epsilon) + 60b^8\,(569 + 1086\epsilon) + 80b^9\,(572 + 1007\epsilon)\\
&\quad + 8b^{10}\,(6721 + 10928\epsilon) + 36b^{11}\,(1639 + 2402\epsilon) + 4b^{12}\,(14877 + 19406\epsilon)\\
&\quad + 105b^{13}\,(497 + 584\epsilon) + 40b^{14}\,(933 + 1016\epsilon) + 800b^{15}\,(26 + 27\epsilon)\\
&\quad + 100b^{16}\,(89 + 90\epsilon) + 2880b^{17}\,(1+\epsilon) + 640b^{18}\,(1+\epsilon) + 80b^{19}\,(1+\epsilon)\big), && (88)\\
\Sigma_{1,2} &= 600b^9\big(5 + 10b + 8b^2 + 6b^3 + 4b^4 + 2b^5\big)^2 \times\\
&\qquad \big(265 + 265b + 34b^2 + 34b^3 + 34b^4 + 34b^5 + 34b^6\big). && (89)
\end{aligned}$$

In the limit $\Gamma \to \infty$ we recover the rigid sphere expressions of Escott and Wilson (2020), as expected.

A general second-order fluid with parameters η, α_0, α_1 in a linear flow field $\mathbf{u}^\infty = \mathbf{E}^\infty \cdot \mathbf{x} + \boldsymbol{\Omega}^\infty \cdot \mathbf{x}$ such as we have imposed, would have homogeneous stress

$$\widehat{\boldsymbol{\Sigma}} = 2\eta\mathbf{E}^\infty + 4\alpha_0\left(\widehat{\mathbf{E}^\infty \cdot \boldsymbol{\Omega}^\infty}\right) + 4(\alpha_0 + \alpha_1)\widehat{\mathbf{E}^\infty \cdot \mathbf{E}^\infty}, \tag{90}$$

meaning that the parameters Σ_0 and Σ_1 govern the effective parameters $\alpha_{0,\mathrm{eff}}$ and $\alpha_{1,\mathrm{eff}}$ for the suspension as a whole:

$$\alpha_{0,\text{eff}} = \frac{\Sigma_0}{4\epsilon}\alpha_0, \qquad \alpha_{1,\text{eff}} = \frac{\Sigma_1 - \Sigma_0}{4}\alpha_1. \tag{91}$$

These govern the behaviour of the normal stress differences in a shearing flow, but the effective viscosity η_{eff} is not affected by terms of order Ca_{e} or order Wi.

The behaviour of the material functions $\alpha_{0,\text{eff}}$ and $\alpha_{1,\text{eff}}$, which govern the behaviour of the whole suspension as a second-order fluid, are explored in figure 14 using cell sizes fit via Krieger–Dougherty $b(\phi)$. We see (as expected) that both material functions increase in magnitude with volume concentration, from a (normalised) value of 1 in the absence of particles up to divergence in the jamming limit. The curves depend much more heavily on Γ than on the fluid parameter ϵ, indicating that there is a real difference between the effects of fluid and solid elasticity here. Indeed the terms $\Sigma_{0,1}$ and $\Sigma_{0,2}$ are independent of ϵ so the only dependence on this fluid parameter comes in through its interaction with deformation; in the case $\Gamma \to \infty$ neither $\alpha_{0,\text{eff}}$ nor $\alpha_{1,\text{eff}}$ varies with ϵ (Escott and Wilson, 2020). As Γ decreases, the rapid increase in the material parameters happens at a lower volume fraction ϕ, such that they can be one or more orders of magnitude larger than those of the pure fluid by a volume fraction as low as 0.4.

5.3. Range of parameter space

We impose limits on our small parameters Ca_{e} and Wi. As mentioned in section 5.1, a comparison with Guido and Shaqfeh (2019) suggests that the Krieger–Dougherty viscosity model is reasonable for $0 \leq \mathit{Ca}_{\text{e}} \leq 0.1$; for consistency we will also keep our Weissenberg number on the same scale, $0 \leq \mathit{Wi} \leq 0.1$. This choice also allows us to make meaningful comparisons with the literature (see section 5.4): the lowest non-zero value of Γ presented in Guido and Shaqfeh (2019) is $\Gamma = 5$, i.e. $\mathit{Ca}_{\text{e}} = \mathit{Wi}/5$; in order to include the Ca_{e} term while neglecting terms of order Wi^2 we require $\mathit{Wi} \ll 0.2$, so $\mathit{Wi} = 0.1$ is close to violating the ordering but still viable. For larger values of Γ we need to take a very small value of Ca_{e} to maintain the condition $\mathit{Wi} \ll 1$.

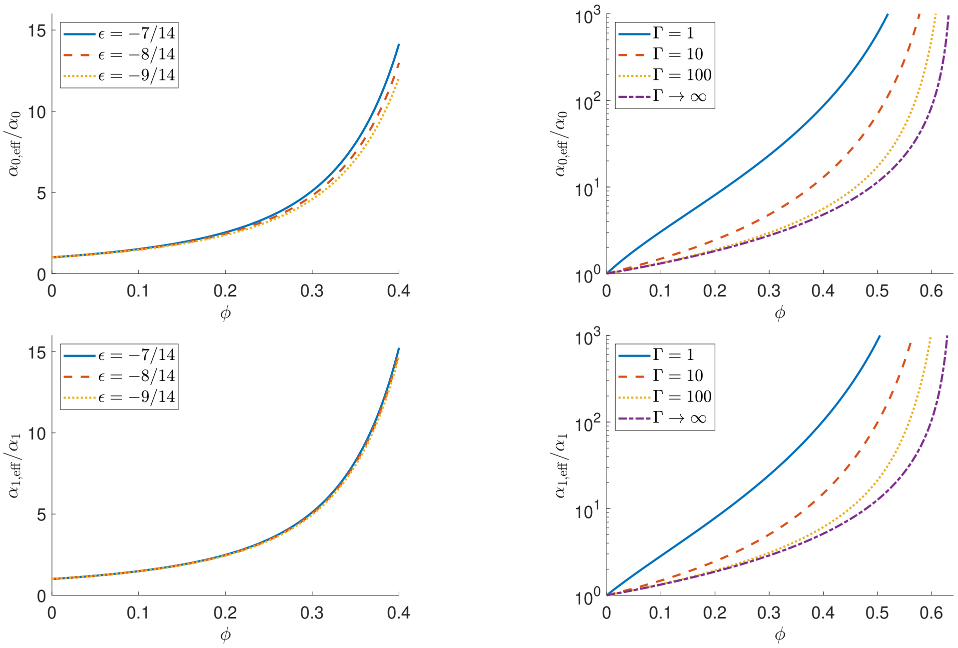

Figure 14: Effective material functions for the suspension, $\alpha_{0,\text{eff}}/\alpha_0$ and $\alpha_{1,\text{eff}}/\alpha_1$, plotted against solid volume fraction ϕ. The call size $b(\phi)$ is set using the Krieger–Dougherty matching function with $\phi_m = 0.64$. Left: $\Gamma = 10$; right: $\epsilon = -8/14$.

We must also bound the range of concentration, ϕ. In uniaxial extensional flow, a comparison of our viscosity with Avazmohammadi and Ponte Castañeda (2016), shown in figure 18 in section 5.5, indicates that our values are within 5% of computational results up to a concentration $\phi = 0.1$. We therefore limit our concentration range to $\phi \in [0, 0.1]$. This reaches beyond the purely dilute limit: the cell model allows us to enter the semi-dilute régime. The KD matching function $b(\phi)$ converts this limit on ϕ into an additional one on the cell size: $b \geq 3$. This is large enough that we need not worry about the potential geometrical constraint in which the deformed particle exceeds the cellular fluid layer.

Finally, we consider the range of ϵ. It is generally accepted (Ho and Leal, 1976) that for real, homogeneous fluids $\epsilon \leq -0.5$. Our fluid is not homogeneous, but it is interesting to ask whether the second-order fluid produced by our homogenisation also satisfies this criterion. For relatively large cell sizes (moderate to large values of b) the constraint is satisfied easily;

in the thin-film limit $b \to 1$, however, matters are more complex.

For finite values of Γ (i.e. nonzero Ca_e, deformable particles) the dominant terms in the expansions of $\alpha_{0,\mathrm{eff}}$ and $\alpha_{1,\mathrm{eff}}$ as $b \to 1$ are:

$$\frac{\alpha_{0,\mathrm{eff}}}{\alpha_0} \sim -\frac{8\phi}{17\Gamma\epsilon(b-1)^6}, \qquad \frac{\alpha_{1,\mathrm{eff}}}{\alpha_1} \sim \frac{24\phi}{119\Gamma(b-1)^7}. \tag{92}$$

These are both positive (note the factor of ϵ in the first term), giving the leading-order behaviour for $\epsilon_\mathrm{eff} = \alpha_{0,\mathrm{eff}}/\alpha_{1,\mathrm{eff}}$ of

$$\epsilon_\mathrm{eff} \sim -\frac{119(b-1)}{51} \tag{93}$$

which does remain in the range $(-\infty, -0.5]$ for all nonzero values of Γ. However, in the special case $\Gamma \to \infty$ (rigid particles) the dominant term in $\alpha_{1,\mathrm{eff}}$ is

$$\frac{\alpha_{1,\mathrm{eff}}}{\alpha_1} = \frac{3\,(9+14\epsilon)\,\phi}{175(b-1)^4} \tag{94}$$

which changes sign at $\epsilon = -9/14$, meaning that for rigid particles only, and for $\epsilon < -9/14$, we could produce a second-order fluid in bulk which lies outside the standard range for homogeneous materials.

5.4. Behaviour in shear flow

We have already fully specified the shear viscosity of our suspension, by matching to the KD form. In this section we present the behaviour of the normal stress differences to complete the shear rheology. The definitions are (for an xy-shear flow $\mathbf{v}^\infty = \dot{\gamma}y\hat{\boldsymbol{x}}$):

$$N_1 = \langle\widehat{\sigma_{xx}}\rangle - \langle\widehat{\sigma_{yy}}\rangle, \qquad N_2 = \langle\widehat{\sigma_{yy}}\rangle - \langle\widehat{\sigma_{zz}}\rangle, \tag{95}$$

and these emerge in terms of the effective material functions as

$$N_1 = -2\epsilon\frac{\alpha_{0,\mathrm{eff}}}{\alpha_0}Wi, \qquad N_2 = \left(\frac{\alpha_{1,\mathrm{eff}}}{\alpha_1} + 2\epsilon\frac{\alpha_{0,\mathrm{eff}}}{\alpha_0}\right)Wi. \tag{96}$$

We present these first and second normal stress differences, normalised by the dimensionless shear stress $\langle\widehat{\sigma_{xy}}\rangle = \eta_\mathrm{eff}/\eta_0$ and by Wi, in figure 15, showing their dependence on the

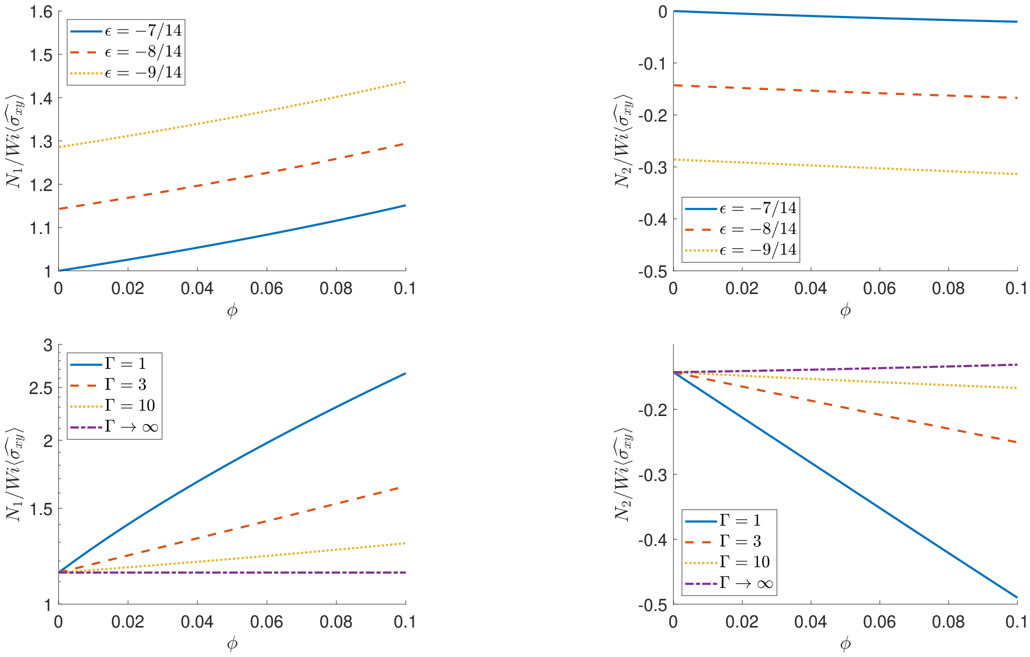

Figure 15: The scaled first and second normal stress differences N_1 (left) and N_2 (right) plotted against solid volume fraction ϕ. For the KD viscosity matching to fix $b(\phi)$ we use $\phi_m = 0.64$. Top: varying ϵ, keeping $\Gamma = 10$. Bottom: varying Γ, keeping $\epsilon = -8/14$.

viscoelastic constant ϵ and the dimensionless parameter ratio Γ. N_1 is positive in all cases, but N_2 is negative at these volume fractions; at a finite value of ϕ (beyond the reasonable limit of our analysis) N_2 changes sign, and both quantities diverge in the positive direction as ϕ approaches the jamming fraction ϕ_m.

The magnitude of both the normal stress differences increases with increasing magnitude of ϵ, and (much more strongly) with decreasing Γ, which corresponds to increasing deformation by increasing Ca_e. We conclude that, at least at these dilute to semi-dilute concentrations, deformation enhances the change to normal stress differences caused by the presence of the particles.

To access the dilute limit, we consider the per-particle contributions to the normal stress differences, ${N_1}'$ and ${N_2}'$, defined in a similar way to ${\eta_\mathrm{eff}}'$ in section 5.1:

$$ {N_1}' = \frac{N_1 - N_1^0}{\phi}, \qquad\qquad {N_2}' = \frac{N_2 - N_2^0}{\phi}. \tag{97} $$

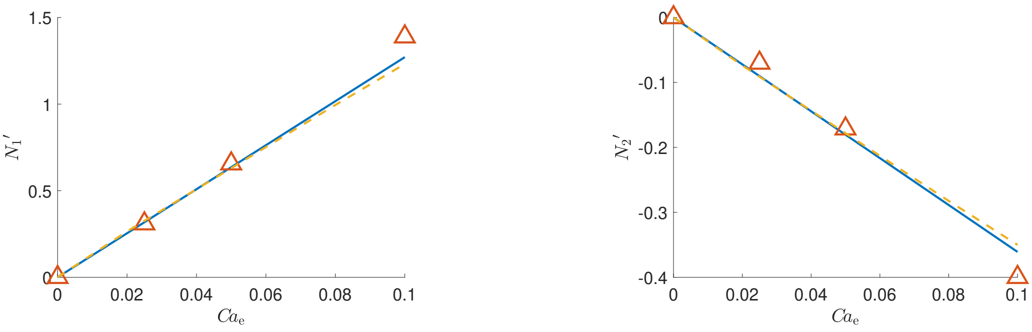

Figure 16: The ϕ coefficient of N_1 and N_2 from equation (97), given a Newtonian background fluid. We use a cell size $b(\phi)$ with a nominal concentration $\phi = 0.0041$. The solid line is our prediction, triangles represent values from figure 8 of Guido and Shaqfeh (2019) and the dashed line shows equivalent results from Gao and Hu (2009).

These quantities are particularly useful for comparison with the available literature; a comparison of our results and those of Guido and Shaqfeh (2019) (computational) and Gao and Hu (2009) (analytical) in a Newtonian background fluid are shown in figure 16. We see excellent agreement, which even extend beyond the values of Ca_e shown here and remains good up to $Ca_\mathrm{e} \approx 0.2$ as long as ϕ is small.

Both normal stress differences increase in magnitude with increasing deformability. This has been seen before (Guido and Shaqfeh, 2019, Villone et al., 2014), and has been understood to be directly related to the inclination angle ζ of the particle. As the elasticity of the solid increases, ζ decreases and the particle becomes more aligned with the flow, enhancing the normal stress differences. However, in our work (as discussed in section 4.4), we have not included enough terms to produce the $O(Ca_\mathrm{e})$ correction to the inclination angle; we deduce that the enhancement to normal stress differences must arise from more than one source and is not entirely caused by a change in particle alignment due to deformation.

We can equally make a direct comparison with the literature (specifically with Guido and Shaqfeh, 2019, which is the seminal work concerning simulations of elastic particles in a viscoelastic fluid) in the case where the suspending fluid is non-Newtonian. In slow-flow conditions any viscoelastic fluid model (which does not have a yield stress) reduces to the

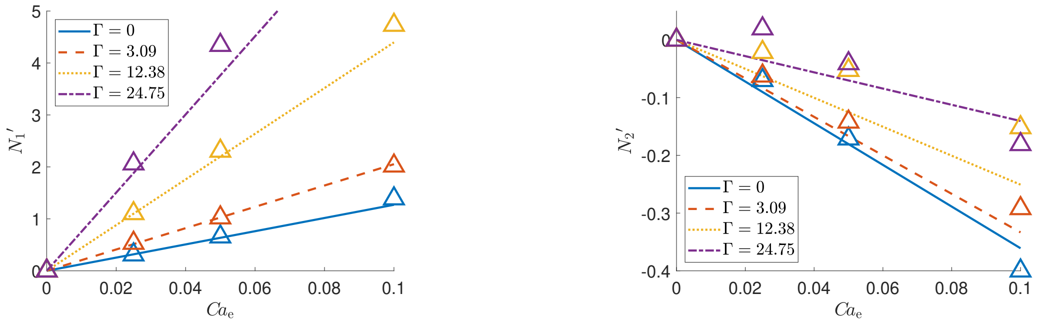

Figure 17: The ϕ coefficient of N_1 and N_2 from equation (97) in a weakly viscoelastic background fluid. The cell size is set by $b(\phi)$ using the nominal value $\phi = 0.0041$. Solid lines represent our predictions, triangles are taken from figure 6 of Guido and Shaqfeh (2019), given a conversion of their Γ values.

second-order fluid, and the Giesekus model used by Guido and Shaqfeh (2019) is no exception. We show this comparison in figure 17, having made the conversions from Giesekus model parameters to second-order fluid material constants. The plots for N_1' show quantitative agreement, and those for N_2' (which is much smaller in magnitude) are qualitatively right, though of course our linear form cannot capture the nonmonotonic dependence on Γ that they see at larger values of Ca_e. Increasing Ca_e increases the magnitude of both quantities; N_1' (which is positive) increases with increasing Γ whereas N_2' (which is negative) is mostly reduced in magnitude by an increase in Γ.

5.5. *Behaviour in extensional flow*

Shear flow, while a useful paradigm (especially in experiments) is not sufficient to fully describe the behaviour of any complex fluid. Rather, extensional rheology is also required to describe the bulk stress and behaviour of solid suspensions. In this section we will discuss the behaviour under uniaxial extension flow, since this can be shown (e.g. Escott and Wilson, 2020) to adequately capture the behaviour under many imposed flows.

As is standard in extensional rheology, we define a (dimensional) far-field velocity (imposed in our case at the outer cell boundary) with rate of extension $\dot{\epsilon}$:

$$\mathbf{v}^{\infty} = \frac{\dot{\epsilon}}{2}(2x, -y, -z), \tag{98}$$

and define the extensional viscosity in dimensional terms as

$$\eta_{\text{ext}} = \frac{1}{\dot{\epsilon}}\left(\langle\widehat{\sigma_{xx}}\rangle - \frac{1}{2}\langle\widehat{\sigma_{yy}}\rangle - \frac{1}{2}\langle\widehat{\sigma_{zz}}\rangle\right). \tag{99}$$

Substituting in our macroscopic equations (82) and (91) and reverting to dimensionless form, we obtain

$$\eta_{\text{ext}} = \frac{3\eta_{\text{eff}}}{\eta_0}\left[1 + \eta_{\text{ext}}^{Wi} Wi\right], \qquad \eta_{\text{ext}}^{Wi} = \frac{\eta_0}{\eta_{\text{eff}}}\left(\frac{\epsilon\alpha_{0,\text{eff}}}{\alpha_0} + \frac{\alpha_{1,\text{eff}}}{\alpha_1}\right), \tag{100}$$

which immediately yield the Trouton ratio Tr:

$$Tr = \frac{\eta_0\eta_{\text{ext}}}{\eta_{\text{eff}}} = 3\left[1 + \eta_{\text{ext}}^{Wi} Wi\right]. \tag{101}$$

In the joint limit $Wi \to 0$, $\Gamma \to \infty$ we correctly regain the result $Tr = 3$ for a Newtonian suspension of undeformable particles, and for a Newtonian fluid with deformable inclusions we agree with Roscoe (1967) in the dilute limit:

$$\frac{\eta_{\text{ext}}}{\eta_{\text{ext}}(\phi = 0)} = 1 + \frac{5\phi}{2} + \frac{75 Ca_{\text{e}}\phi}{28} \quad \text{as} \quad \phi \to 0. \tag{102}$$

The ϕ-coefficient above $(5/2 + 75Ca_{\text{e}}/28)$ agrees well with the seminal paper of Gao et al. (2013) in the case where their particles are initially spherical: we do not have the ability to make comparisons with their study of other particles due to differing initial aspect ratios.

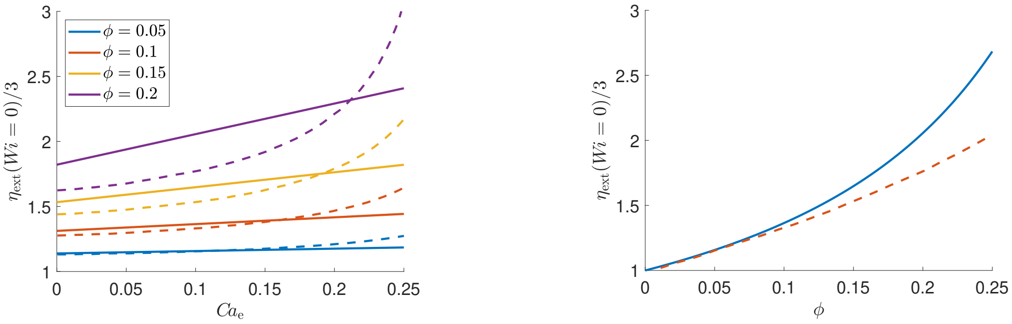

Figure 18: The normalised extensional viscosity η_{ext} in Newtonian background fluid. Left: dependence on Ca_{e} at fixed values of ϕ (bottom to top: $\phi = 0.05$, 0.1, 0.15, 0.2); right: dependence on ϕ for fixed $Ca_{\text{e}} = 0.1$. Our analysis: solid lines; dashed lines from Avazmohammadi and Ponte Castañeda (2016).

As the dilute result above implies, there is a nonzero dependence of extensional viscosity on deformation even in the Newtonian limit. In figure 18 we show the dependence of the extensional viscosity on both Ca_e and the volume fraction ϕ, for a Newtonian fluid, and in comparison with numerical results from Avazmohammadi and Ponte Castañeda (2016). That work uses both neo-Hookean and Gent models for the solid phase; we use their results for the neo-Hookean model. Note that in this figure we show results for a wider range of Ca_e and ϕ than used elsewhere, precisely to show which regions of parameter space start to show a serious deviation from computational results (in order to limit the parameter values for which we will trust our analysis to be representative of reality, as described in section 5.3).

We see that our trend against elastic capillary number is not convincing, as we do not capture the increase in η_ext with increasing Ca_e seen in the computational results. The likely cause is a combination of the weaknesses of the cell model at finite values of ϕ, and the neglected higher-order terms in the expansion for Ca_e. The overall trend against volume fraction is good, especially for low ϕ; at larger $\phi \geq 0.25$ (beyond the range shown) we predict a strain-thinning behaviour which is at odds with the literature. This is a hard upper limit on the volume fractions for which we believe our model to be appropriate.

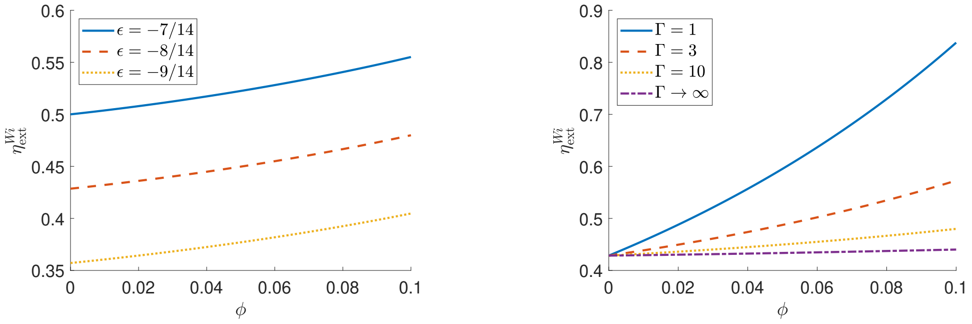

Figure 19: η_ext^{Wi}, the $O(Wi)$ coefficient of extensional viscosity η_ext in a uniaxial extension flow. The coefficient is scaled by 3 and the dimensionless effective shear viscosity η_eff/η_0, with chosen jamming fraction $\phi_m = 0.64$. Left: $\Gamma = 10$, varying ϵ. Right: $\epsilon = -8/14$, varying Γ.

There is much less literature available for suspensions with a non-Newtonian suspending fluid; the combination with extensional flow is essentially uncharted territory, so our results are presented without any comparisons. In figure 19, we plot η_{ext}^{Wi} from equation (100) against solid volume fraction ϕ. We see that increasing the magnitude of the viscoelastic constant ϵ leads to a slight reduction in the effective viscosity, whereas the extensional viscosity increases strongly with a decrease in Γ.

6. Conclusions

In this paper we have presented a method of deriving the rheology of a suspension of weakly deformable spheres in a weakly viscoelastic fluid, at low to moderate values of the volume fraction ϕ. Our calculations are based on small-deformation (for the solid) and small-elasticity expansions (for the fluid), and we use a cell model to extend a mean-field single-sphere analysis for validity beyond the strictly dilute limit. The whole suspension behaves as a second-order fluid having different material parameters from the suspending fluid: thus, we can describe the rheology in different flow scenarios (shear, extension, etc.) through just three scalar parameters η_{eff}, $\alpha_{0,\text{eff}}$ and $\alpha_{1,\text{eff}}$, each of which depends on all the physical parameters of the suspension (suspending fluid parameters, solid deformability, and volume fraction). From these we have derived normal stress differences in shear flow (section 5.4) and viscosity in uniaxial extension (section 5.5).

We have derived solutions for the velocities $\mathbf{v}$ and $\overline{\mathbf{v}}$, found in the fluid and elastic solid phases respectively, in addition to the pressure-like terms p and l. There are four sets of these solutions, each representing one order of our perturbation series. The leading-order solutions describe rigid inclusions in a Newtonian fluid; here the full solutions for a given far-field flow are given by equation (52) using the constants presented in equations (53–56). The first correction for fluid viscoelasticity, the $O(Wi)$ term, is discussed in section 3.2. The main solution is equation (57) using constants presented in Appendix A.

The next consideration at a local level is the deformation (presented in section 3.3), which sets this work apart from our earlier study (Escott and Wilson, 2020). Again, we have the specific tensorial profiles (61–62), with solutions presented in Appendix B. At this order of calculation, we can start to investigate the change in shape of the single solid particle, and other measures associated with deformation, such as the Taylor parameter (equation (68)). Finally, we calculate a few quantities (notably particle shape) at the first order where fluid elasticity and particle deformation interact; this allows us to calculate the angle of inclination in shear flow (section 4.4). We find that fluid elasticity acts to decrease the inclination angle, enhancing the effects of deformation.

One of the major subtleties of the cell model is the relation between the cell radius b and the solid volume fraction ϕ. We have chosen a relation which ensures that the shear viscosity behaves correctly for a Newtonian suspension of rigid spheres, using the Krieger-Dougherty relation. The addition of weak viscoelasticity or weak deformability could, of course, change the inter-particle spatial distribution in a suspension; however, the computations of Shaqfeh (2019) for rigid particles in a viscoelastic liquid and Guido and Shaqfeh (2019) for deformable particles in a viscoelastic liquid suggest that the particle-induced fluid stress is remarkably unaffected by these effects, suggesting that the spatial distribution may be robust to at least small changes. It is perhaps more difficult to be certain about the applicability of our relation for non-shearing flows.

We have validated our analytical calculations against literature for rigid spheres in a weakly viscoelastic fluid and for deformable spheres in a Newtonian fluid, and the parameter ranges over which we trust our results are derived from a comparison with various numerical simulations in the literature. Our model should be useful in the range $Wi \leq 0.1$, $Ca_{\mathrm{e}} \leq 0.1$, $\phi \leq 0.1$; when making comparisons with the literature (for which the material parameter $\Gamma = Wi/Ca_{\mathrm{e}}$ is often set at 5 or larger) we sometimes require slightly smaller values of Ca_{e} to ensure that the neglected term at order Wi^2 is not larger than the terms we have retained.

Our predictions for extensional rheology (section 5.5) are comparable to simulations in Newtonian fluids (Avazmohammadi and Ponte Castañeda, 2015) up to surprisingly large deformations $Ca_{\mathrm{e}} \approx 0.2$; the addition of viscoelasticity always increases the extensional viscosity of the suspension, a stronger effect than that of deformability.

Overall, we have produced a constitutive model for a suspension of deformable particles in a viscoelastic fluid which, while arduous to derive, is exceptionally simple to use numerically since it is just a modified second-order fluid. In order to use the model in simulations, a researcher must first determine the relevant value of the cell radius b from the volume fraction ϕ, either by equating equations (78) and (79) and solving numerically or by using the tabulated values given in Escott and Wilson (2020). The viscosity η_{eff} is simply given by the Krieger–Dougherty relation in equation (79) and the two second-order fluid parameters are given, in terms of the physical parameters of the system and the cell radius b, by equation (91) with the expressions for Σ_0 and Σ_1 defined in equations (84–89).

Our model is capable of reproducing, at least qualitatively, some of the first effects of the interaction between deformation and viscoelasticity. It also allows us to qualitatively capture the effects of confinement ratio (as in Villone et al., 2014) on various quantities including the angle of inclination in shear flow, the Taylor parameter and the Trouton ratio.

Several avenues for future work naturally arise from this study, including particle size polydispersity, and the possibility to embed cell model calculations within numerical simulations. The calculation method could be extended by considering cells containing two particles, and thereby allow the potential to incorporate solid-solid interactions: this would build on the analytical solution of Lin et al. (1970) for the motion of two rigid spheres in unbounded shear flow of a Newtonian fluid.

Acknowledgements

This work was supported by EPSRC Grant EP/N024915/1. In addition, one author (HJW) would like to thank the Isaac Newton Institute for Mathematical Sciences, Cambridge, for support and hospitality during the programme *New statistical physics in living matter: non equilibrium states under adaptive control*, where work on this paper was undertaken. This work was supported by EPSRC grant no EP/R014604/1.

References

Adams, S., Frith, W.J., Stokes, J.R., 2004. Influence of particle modulus on the rheological properties of agar microgel suspensions. J. Rheol. 48, 1195–1213. doi: 10.1122/1.1795193.

Amini, K. Martensson, G. Tammisola, O. Lundell, F. 2022. Experimental Investigation on Particle-Laden Flows of Viscoelastic Fluids in Micro-Channels Using Optical Coherence Tomography. Annual Transactions of the Nordic Rheology Society 30.

Ardekani, A.M., Rangel, R.H., 2008. Numerical investigation of particle–particle and particle–wall collisions in a viscous fluid. J. Fluid Mech. 596, 437–466. doi: 10.1017/S0022112007009688.

Avazmohammadi, R., Ponte Castañeda, P., 2015. The rheology of non-dilute dispersions of highly deformable viscoelastic particles in Newtonian fluids. J. Fluid Mech. 763, 386–432. doi: 10.1017/jfm.2014.687.

Avazmohammadi, R., Ponte Castañeda, P., 2016. Macroscopic rheological behavior of suspensions of soft solid particles in yield stress fluids. J. Non-Newt. Fluid Mech. 234, 139–161. doi: 10.1016/j.jnnfm.2016.05.005.

Barthès-Biesel, D., 1980. Motion of a spherical microcapsule freely suspended in a linear shear flow. J. Fluid Mech. 100, 831–853. doi: 10.1017/S0022112080001449.

Barthès-Biesel, D., Rallison, J., 1981. The time-dependent deformation of a capsule freely suspended in a linear shear flow. J. Fluid Mech. 113, 251–267. doi: 10.1017/S0022112081003480.

Batchelor, G.K., Green, J.T., 1972. The determination of the bulk stress in a suspension of spherical particles to order c^2. J. Fluid Mech. 56, 401–427. doi: 10.1017/S0022112072002435.

Bergström, L., 1998. Shear thinning and shear thickening of concentrated ceramic suspensions. Colloids Surf. A 133, 151–155. doi: 10.1016/S0927-7757(97)00133-7.

Bretherton, F.P., 1962. The motion of rigid particles in a shear flow at low Reynolds number. J. Fluid Mech.. 14, 284–304. doi: 10.1017/S002211206200124X.

Chien, S., 1987. Red cell deformability and its relevance to blood flow. Ann. Rev. Physiology 49, 177–192. doi: 10.1146/annurev.ph.49.030187.001141.

Clausen, J.R., Aidun, C.K., 2010. Capsule dynamics and rheology in shear flow: Particle pressure and normal stress. Phys. Fluids 22, 123302. doi: 10.1063/1.3483207.

Dai, S., Qi, F., Tanner, R.I., 2014. Viscometric functions of concentrated non-colloidal suspensions of spheres in a viscoelastic matrix. J. Rheol. 58, 183–198. doi: 10.1122/1.4851336.

Einarsson, J., Yang, M., Shaqfeh, E.S.G., 2017. The Einstein viscosity with fluid elasticity. Phys. Rev. Fluids 3, 013301. doi: 10.1103/PhysRevFluids.3.013301.

Einstein, A., 1906. Eine neue Bestimmung der Moleküldimensionen. Annalen der Physik 324, 289–306. doi: 10.1002/andp.19063240204.

Escott, L.J., 2021. The rheology of weakly-viscoelastic multiphase systems using a cell model. Ph.D. thesis. UCL. URL: `https://discovery.ucl.ac.uk/id/eprint/10151771`.

Escott, L.J., Wilson, H.J., 2020. Investigation into the rheology of a solid sphere suspension in second-order fluid using a cell model. Phys. Rev. Fluids 5, 83301. doi: 10.1103/PhysRevFluids.5.083301.

Fernandez, N., Mani, R., Rinaldi, D., Kadau, D., Mosquet, M., Lombois-Burger, H., Cayer-Barrioz, J., Herrman, H.J., Spencer, N.D., Isa, L., 2013. Microscopic mechanism for shear thickening of non-Brownian suspensions. Phys. Rev. Lett. 111, 108301. doi: 10.1103/PhysRevLett.111.108301.

Fröhlich, H., Sack, R., 1946. Theory of the rheological properties of dispersions. Proc. Roy. Soc. A 185, 415–430. doi: 10.1098/rspa.1946.0028.

Gao, T., Hu, H.H., 2009. Deformation of elastic particles in viscous shear flow. J. Comp. Phys. 228, 2132–2151. doi: 10.1016/j.jcp.2008.11.029.

Gao, T., Hu, H.H., Castañeda, P.P., 2012. Shape dynamics and rheology of soft elastic particles in a shear flow. Phys. Rev. Lett. 108, 058302. doi: 10.1103/PhysRevLett.108.058302.

Gao, T., Hu, H.H., Castañeda, P.P., 2013. Dynamics and rheology of elastic particles in an extensional flow. J. Fluid Mech. 715, 573–596. doi: 10.1017/jfm.2012.536.

Goddard, J.D., Miller, C., 1967. Nonlinear effects in the rheology of dilute suspensions. J. Fluid Mech. 28, 657–673. doi: 10.1017/S0022112067002381.

Greco, F., D'Avino, G., Maffettone, P.L., 2007. Rheology of a dilute suspension of rigid spheres in a second order fluid. J. Non-Newt. Fluid Mech. 147, 1–10. doi: 10.1016/j.jnnfm.2007.06.002.

Guido, C.J., Shaqfeh, E.S., 2019. The rheology of soft bodies suspended in the simple shear flow of a viscoelastic fluid. J. Non-Newt. Fluid Mech. 273, 104183. doi: 10.1016/j.jnnfm.2019.104183.

Happel, J., 1957. Viscosity of suspensions of uniform spheres. J. Appl. Phys. 28, 1288–1292. doi: 10.1063/1.1722635.

Ho, B.P., Leal, L.G., 1976. Migration of rigid spheres in a two-dimensional unidirectional shear flow of a second-order fluid. J. Fluid Mech. 76, 783–799. doi: 10.1017/S002211207600089X.

Housiadas, K.D., Tanner, R.I., 2009. On the rheology of a dilute suspension of rigid spheres in a weakly viscoelastic matrix fluid. J. Non-Newt. Fluid Mech. 162, 88–92. doi: 10.1016/j.jnnfm.2009.05.006.

Howell, P., Kozyreff, G., Ockendon, J., 2009. Applied Solid Mechanics. Cambridge University Press. doi: 10.1017/CBO9780511611605.

Hwang, W.R., Hulsen, M.A., Meijer, H.E.H., Kwon, T.H., 2004. Direct numerical simulations of suspensions of spherical particles in a viscoelastic Fluid in sliding tri-periodic domains in: Proc. XIVth Int. Congr. on Rheology Seoul 22–27.

Jaensson, N.O., Hulsen, M.A., Anderson, P.D., 2015. Simulations of the start-up of shear flow of 2D particle suspensions in viscoelastic fluids: Structure formation and rheology J. Non-Newt. Fluid Mech. 225, 70–85. doi: 10.1016/j.jnnfm.2015.09.006.

Jeffery, G.B., 1922. The motion of ellipsoidal particles immersed in a viscous fluid. Proc. Roy. Soc. A 102, 161–179. doi: 10.1098/rspa.1922.0078.

Kaloni, P.N., Statsna, V., 1983. Steady-shear rheological behavior of the suspension of spherical particles in a second-order fluid. Polym. Eng. Sci. 23, 465–470. doi: 10.1002/pen.760230809.

Keller, S.R., Skalak, R., 1982. Motion of a tank-treading ellipsoidal particle in a shear flow. J. Fluid Mech. 120, 27–47. doi: 10.1017/S0022112082002651.

Koch, D.L., Subramanian, G., 2006. The stress in a dilute suspension of spheres suspended in a second-order fluid subject to a linear velocity field. J. Non-Newt. Fluid Mech. 138, 87–97. doi: 10.1016/j.jnnfm.2006.03.019.

Koch, D.L., Subramanian, G., 2008. Corrigendum to "The stress in a dilute suspension of spheres suspended in a second-order fluid subject to a linear velocity field". J. Non-Newt. Fluid Mech. 153, 202. doi: 10.1016/j.jnnfm.2006.03.019.

Le, D.V., Khoo, B.C., Peraire, J., 2006. An immersed interface method for viscous incompressible flows involving rigid and flexible boundaries. J. Comp. Phys. 220, 109–138. doi: 10.1016/j.jcp.2006.05.004.

Lin, C., Lee, K., Sather, N., 1970. Slow motion of two spheres in a shear field. J. Fluid Mech. 43, 35–47. doi: 10.1017/S0022112070002227.

Liu, A.J., Nagel, S.R., 2001. Jamming and rheology: constrained dynamics on microscopic and macroscopic scales. CRC Press.

Malidi, A., Harlen, O., 2008. Numerical simulations of suspensions of elastic particles in polymer melts. AIP Conf. Proc. 1027, 641–643. doi: 10.1063/1.2964793.

Matsunaga, D., Imai, Y., Yamaguchi, T., Ishikawa, T., 2016. Rheology of a dense suspension of spherical capsules under simple shear flow. J. Fluid Mech. 786, 110–127. doi: 10.1017/jfm.2015.666.

Mifflin, R.T., 1985. Dissipation in a dilute suspension of spheres in a second-order fluid. J. Non-Newt. Fluid Mech. 17, 267–274. doi: 10.1016/0377-0257(85)80021-5.

Murata, T., 1981. Deformation of an elastic particle suspended in an arbitrary flow field. J. Phys. Soc. Japan 50, 1009–1016. doi: 10.1143/JPSJ.50.1009.

Patankar, N.A., Hu, H.H., 2001. Rheology of a suspension of particles in viscoelastic fluids. J. Non-Newt. Fluid Mech. 96, 427–443. doi: 10.1016/S0377-0257(00)00154-3.

Pozrikidis, C., 1992. Boundary integral and singularity methods for linearized viscous flow. Cambridge University Press.

Rallison, J.M., 2012. The stress in a dilute suspension of liquid spheres in a second-order fluid. J. Fluid Mech. 693, 500–507. doi: 10.1017/jfm.2011.544.

Rivlin, R.S., Ericksen, J.L., 1955. Stress-deformation relations for isotropic materials. J. Rat. Mech. Anal. 4, 323–425. URL: `https://www.jstor.org/stable/24900365`.

Roscoe, R., 1967. On the rheology of a suspension of viscoelastic spheres in a viscous liquid. J. Fluid Mech. 28, 273–293. doi: 10.1017/S002211206700206X.

Rosti, M.E., Brandt, L., Mitra, D., 2018. Rheology of suspensions of viscoelastic spheres: Deformability as an effective volume fraction. Phys. Rev. Fluids 3, 1–7. doi: 10.1103/PhysRevFluids.3.012301.

Seto, R., Giusteri, G.G., Martiniello, A., 2017. Microstructure and thickening of dense suspensions under extensional and shear flows. J. Fluid Mech. 825, R3. doi: 10.1017/jfm.2017.469.

Shaqfeh, E.S.G., 2019. On the rheology of particle suspensions in viscoelastic fluids. A.I.Ch.E.J. 65, e16575. doi: 10.1002/aic.16575.

Sherwood, J.D., 2006. Cell models for suspension viscosity. Chem. Eng. Sci. 61, 6727–6731. doi: 10.1016/j.ces.2006.07.016.

Simha, R., 1952. A treatment of the viscosity of concentrated suspensions. J. Appl. Phys. 23, 1020–1024. doi: 10.1063/1.1702338.

Sui, Y., Low, H.T., Chew, Y.T., Roy, P., 2008. Tank-treading, swinging, and tumbling of liquid-filled elastic capsules in shear flow. Phys. Rev. E 77, 1–10. doi: 10.1103/PhysRevE.77.016310.

Villone, M.M., 2019. Lateral migration of deformable particles in microfluidic channel flow of Newtonian and viscoelastic media: a computational study. Microfluid. Nanofluid. 23, 1–13. doi: 10.1007/s10404-019-2212-3.

Villone, M.M., Greco, F., Hulsen, M.A., Maffettone, P.L., 2014. Simulations of an elastic particle in Newtonian and viscoelastic fluids subjected to confined shear flow. J. Non-Newt. Fluid Mech. 210, 47–55. doi: 10.1016/j.jnnfm.2014.05.003.

Villone, M.M., Nunes, J.K., Li, Y., Stone, H.A., Maffettone, P.L., 2019. Design of a microfluidic device for the measurement of the elastic modulus of deformable particles. Soft Matter 15, 880–889. doi: 10.1039/c8sm02272k.

Wyart, M., Cates, M.E., 2014. Discontinuous shear thickening without inertia in dense non-Brownian suspensions. Phys. Rev. Lett. 112, 98302. doi: 10.1103/PhysRevLett.112.098302.

Xu, X., Rice, S.A., Dinner, A.R., 2013. Relation between ordering and shear thinning in colloidal suspensions. Proc. Natl Acad. Sci. U.S.A. 110, 1–6. doi: 10.1073/pnas.1301055110.

Yang, M., Krishnan, S., Shaqfeh, E.S.G., 2016. Numerical simulations of the rheology of suspensions of rigid spheres at low volume fraction in a viscoelastic fluid under shear. J. Non-Newt. Fluid Mech. 234, 51–68. doi: 10.1016/j.jnnfm.2016.04.003.

Yang, M., Shaqfeh, E.S.G., 2018a. Mechanism of shear thickening in suspensions of rigid spheres in Boger fluids. Part I: Dilute suspensions. J. Rheol. 1363. doi: 10.1122/1.5024696.

Yang, M., Shaqfeh, E.S.G., 2018b. Mechanism of shear thickening in suspensions of rigid spheres in Boger fluids. Part II: Suspensions at finite concentration. J. Rheol. 62, 1363–1377. doi: 10.1122/1.5024698.

Zhang, L., Gerstenberger, A., Wang, X., Liu, W.K., 2004. Immersed finite element method. Comp. Meth. Appl. Mech. Engg 193, 2051–2067. doi: 10.1016/j.cma.2003.12.044.

Zhang, L.T., Gay, M., 2007. Immersed finite element method for fluid–structure interactions. J. Fluids Struct. 23, 839–857. doi: 10.1016/j.jfluidstructs.2007.01.001.

Appendix A. Asymptotic expansions at order *Wi*

The solutions for velocity and pressure at order Weissenberg number are given in general form in equation (57) in terms of the background tensors $\mathbf{E}^\infty$ and $\mathbf{\Omega}^\infty$ and the unit vector $\hat{\mathbf{n}}$ and unknown radial functions $V_n^{1Wi}(r)$ (for $n = 1, \dots 9$) and $P_n^{1Wi}(r)$ (for $n = 1, \dots 3$). The equations governing the order-Wi spherical functions are linear in the variables $V_n^{1,Wi}$ and $P_n^{1,Wi}$, which means their solutions can be split into homogeneous and particular solutions:

$$V_n^{1Wi} = W_{n,hom}^{1Wi} + V_{n,par}^{1Wi}, \qquad P_n^{1Wi} = Q_{n,hom}^{1Wi} + P_{n,par}^{1Wi}, \tag{A.1}$$

(a useful construction because the homogeneous solutions will appear in later calculations).

The general solutions for fluid velocity, as functions of r and incorporating constants yet to be found, are:

$$W_{1,hom}^{1Wi} = C_1^{1Wi} r^5 + \frac{C_2^{1Wi}}{r^6} + \frac{C_{19}^{1Wi}}{2r^4}, \tag{A.2}$$

$$W_{2,hom}^{1Wi} = -\frac{4C_1^{1Wi} r^5}{9} - \frac{4C_2^{1Wi}}{9r^6} + C_3^{1Wi} r^3 + \frac{C_4^{1Wi}}{r^4} - \frac{4C_{20}^{1Wi} r^5}{63} + \frac{C_{21}^{1Wi}}{2r^2}, \tag{A.3}$$

$$\begin{aligned} W_{3,hom}^{1Wi} = \frac{2C_1^{1Wi} r^5}{63} + \frac{2C_2^{1Wi}}{63r^6} - \frac{C_3^{1Wi} r^3}{5} - \frac{C_4^{1Wi}}{5r^4} + C_5^{1Wi} r + \frac{C_6^{1Wi}}{r^2} - \frac{C_{19}^{1Wi}}{35r^4} \\ + \frac{4C_{20}^{1Wi} r^5}{315} - \frac{C_{22}^{1Wi} r^3}{15} + \frac{C_{23}^{1Wi}}{2}, \end{aligned} \tag{A.4}$$

$$W_{4,hom}^{1Wi} = -\frac{4C_1^{1Wi} r^5}{9} - \frac{4C_2^{1Wi}}{9r^6} + C_7^{1Wi} r^3 + \frac{C_8^{1Wi}}{r^4} + \frac{2C_{20}^{1Wi} r^5}{9}, \tag{A.5}$$

$$\begin{aligned} W_{5,hom}^{1Wi} = \frac{8C_1^{1Wi} r^5}{63} + \frac{8C_2^{1Wi}}{63r^6} - \frac{2C_3^{1Wi} r^3}{5} - \frac{2C_4^{1Wi}}{5r^4} - \frac{2C_7^{1Wi} r^3}{5} - \frac{2C_8^{1Wi}}{5r^4} \\ + C_9^{1Wi} r + \frac{C_{10}^{1Wi}}{r^2} - \frac{4C_{19}^{1Wi}}{35r^4} - \frac{4C_{20}^{1Wi} r^5}{63} + \frac{C_{22}^{1Wi} r^3}{5}, \end{aligned} \tag{A.6}$$

$$W_{6,hom}^{1Wi} = C_{11}^{1Wi} r^3 + \frac{C_{12}^{1Wi}}{r^4} + \frac{C_{26}^{1Wi}}{2r^2}, \qquad W_{7,hom}^{1Wi}(r) = C_{13}^{1Wi} r^3 + \frac{C_{14}^{1Wi}}{r^4}, \tag{A.7}$$

$$W_{8,hom}^{1Wi} = -\frac{C_{11}^{1Wi} r^3}{5} - \frac{C_{12}^{1Wi}}{5r^4} + C_{15}^{1Wi} r + \frac{C_{16}^{1Wi}}{r^2} + \frac{C_{25}^{1Wi} r^3}{10}, \tag{A.8}$$

$$W_{9,hom}^{1Wi} = \frac{C_{11}^{1Wi} r^3}{5} + \frac{C_{12}^{1Wi}}{5r^4} - \frac{2C_{13}^{1Wi} r^3}{5} - \frac{2C_{14}^{1Wi}}{5r^4} + C_{17}^{1Wi} r + \frac{C_{18}^{1Wi}}{r^2} - \frac{C_{25}^{1Wi} r^3}{10}. \tag{A.9}$$

Those for the fluid pressure are:

$$Q_{1,hom}^{1Wi} = \frac{C_{19}^{1Wi}}{r^5} + C_{20}^{1Wi} r^4, \tag{A.10}$$

$$Q_{2,hom}^{1Wi} = -\frac{4C_{19}^{1Wi}}{7r^5} - \frac{4C_{20}^{1Wi} r^4}{7} + \frac{C_{21}^{1Wi}}{r^3} + C_{22}^{1Wi} r^2, \tag{A.11}$$

$$Q_{3,hom}^{1Wi} = \frac{2C_{19}^{1Wi}}{35r^5} + \frac{2C_{20}^{1Wi} r^4}{35} - \frac{C_{21}^{1Wi}}{3r^3} - \frac{C_{22}^{1Wi} r^2}{3} + \frac{C_{23}^{1Wi}}{r} + C_{24}^{1Wi}, \tag{A.12}$$

$$Q_{4,hom}^{1Wi} = C_{25}^{1Wi} r^2 + \frac{C_{26}^{1Wi}}{r^3}. \tag{A.13}$$

Note that the constant C_{24}^{1Wi} simply applies an arbitrary constant pressure to the whole system; we need not solve for it and will neglect it in the remaining analysis.

The particular solutions V_{par}^{1Wi} and P_{par}^{1Wi} can be found by solving the forced differential equations. The scalar velocity functions are

$$\begin{aligned} V_{1,par}^{1Wi}\left(r\right) = &-\frac{735\left(2+3\epsilon\right)\left(C_1^0\right)^2}{8r^4} - \frac{175\left(1+\epsilon\right)\left(C_1^0\right)^2}{8r^2} + \frac{25\left(1+\epsilon\right)C_1^0C_2^0}{r^7} + \frac{875\left(2+3\epsilon\right)C_1^0C_2^0}{8r^4} \\ &+ \frac{175\left(1+\epsilon\right)C_1^0C_2^0}{8r^2} + \frac{275\left(1+\epsilon\right)C_1^0C_2^0}{24} + \frac{50\left(1+\epsilon\right)\left(C_2^0\right)^2}{r^5} - \frac{275\left(1+\epsilon\right)\left(C_2^0\right)^2}{24}, \end{aligned} \tag{A.14}$$

$$\begin{aligned} V_{2,par}^{1Wi}\left(r\right) = &\frac{5\left(46+55\epsilon\right)\left(C_1^0\right)^2}{28r^2} + \frac{25\left(53+27\epsilon\right)\left(C_1^0\right)^2r^5}{84} - \frac{5\left(1+\epsilon\right)C_1^0C_2^0}{r^7} \\ &- \frac{5\left(67-50\epsilon\right)C_1^0C_2^0}{28r^2} + \frac{425\left(1+\epsilon\right)C_1^0C_2^0}{36} - \frac{25\left(53+27\epsilon\right)C_1^0C_2^0r^5}{42} - \frac{75\left(1+\epsilon\right)\left(C_2^0\right)^2}{2r^5} \\ &+ \frac{125\left(1-5\epsilon\right)\left(C_2^0\right)^2}{28r^2} - \frac{425\left(1+\epsilon\right)\left(C_2^0\right)^2}{36} + \frac{25\left(53+27\epsilon\right)\left(C_2^0\right)^2r^5}{84}, \end{aligned} \tag{A.15}$$

$$\begin{aligned} V_{3,par}^{1Wi}\left(r\right) = &\frac{21\left(2+3\epsilon\right)\left(C_1^0\right)^2}{4r^4} - \frac{21\left(11+20\epsilon\right)\left(C_1^0\right)^2r^3}{8} + \frac{5\left(83+135\epsilon\right)\left(C_1^0\right)^2r^5}{168} \\ &- \frac{25\left(2+3\epsilon\right)C_1^0C_2^0}{4r^4} - \frac{10\left(4-5\epsilon\right)C_1^0C_2^0}{9} + \frac{23\left(11+20\epsilon\right)C_1^0C_2^0r^3}{4} \\ &- \frac{5\left(83+135\epsilon\right)C_1^0C_2^0r^5}{84} + \frac{25\left(1+\epsilon\right)\left(C_2^0\right)^2}{6r^5} + \frac{10\left(4-5\epsilon\right)\left(C_2^0\right)^2}{9} \\ &- \frac{25\left(11+20\epsilon\right)\left(C_2^0\right)^2r^3}{8} + \frac{5\left(83+135\epsilon\right)\left(C_2^0\right)^2r^5}{168}, \end{aligned} \tag{A.16}$$

$$\begin{aligned} V_{4,par}^{1Wi}\left(r\right) = &-\frac{25\left(11-15\epsilon\right)\left(C_1^0\right)^2r^5}{24} - \frac{25\left(1+\epsilon\right)C_1^0C_2^0}{2r^7} + \frac{275\left(1+\epsilon\right)C_1^0C_2^0}{36} \\ &+ \frac{25\left(11-15\epsilon\right)C_1^0C_2^0r^5}{12} - \frac{75\left(1+\epsilon\right)\left(C_2^0\right)^2}{4r^5} - \frac{275\left(1+\epsilon\right)\left(C_2^0\right)^2}{36} - \frac{25\left(11-15\epsilon\right)\left(C_2^0\right)^2r^5}{24}, \end{aligned} \tag{A.17}$$

$$\begin{aligned}V^{1Wi}_{5,par}\left(r\right) = {} & \frac{21\left(2+3\epsilon\right)\left(C^0_1\right)^2}{r^4} + \frac{63\left(11+20\epsilon\right)\left(C^0_1\right)^2 r^3}{8} - \frac{25\left(125+177\epsilon\right)\left(C^0_1\right)^2 r^5}{168} \\ & - \frac{25\left(2+3\epsilon\right)C^0_1 C^0_2}{r^4} + \frac{350\left(1+\epsilon\right)C^0_1 C^0_2}{9} - \frac{69\left(11+20\epsilon\right)C^0_1 C^0_2 r^3}{4} \\ & + \frac{25\left(125+177\epsilon\right)C^0_1 C^0_2 r^5}{84} + \frac{25\left(1+\epsilon\right)\left(C^0_2\right)^2}{2r^5} - \frac{350\left(1+\epsilon\right)\left(C^0_2\right)^2}{9} \\ & + \frac{75\left(11+20\epsilon\right)\left(C^0_2\right)^2 r^3}{8} - \frac{25\left(125+177\epsilon\right)\left(C^0_2\right)^2 r^5}{168}, \end{aligned} \tag{A.18}$$

$$V^{1Wi}_{6,par}\left(r\right) = -\frac{5\epsilon C^0_2}{r^2}, \qquad V^{1Wi}_{7,par}\left(r\right) = 0, \tag{A.19}$$

$$V^{1Wi}_{8,par}\left(r\right) = \frac{21\epsilon C^0_1 r^3}{4} - \frac{21\epsilon C^0_2 r^3}{4}, \qquad V^{1Wi}_{9,par}\left(r\right) = -\frac{21\epsilon C^0_1 r^3}{4} + \frac{21\epsilon C^0_2 r^3}{4}, \tag{A.20}$$

with pressure functions

$$\begin{aligned}P^{1Wi}_{1,par}\left(r\right) = {} & \frac{45\left(2+3\epsilon\right)\left(C^0_1\right)^2}{2r^{10}} - \frac{25\left(59+78\epsilon\right)\left(C^0_1\right)^2}{2r^3} - \frac{25\left(8+11\epsilon\right)C^0_1 C^0_2}{2r^8} \\ & + \frac{25\left(19+18\epsilon\right)C^0_1 C^0_2}{r^3} + \frac{25\left(79+120\epsilon\right)C^0_1 C^0_2}{4r} + \frac{25\left(6+5\epsilon\right)\left(C^0_2\right)^2}{2r^6} \\ & + \frac{625\left(1+2\epsilon\right)\left(C^0_2\right)^2}{2r^3} - \frac{25\left(79+120\epsilon\right)\left(C^0_2\right)^2}{4r},\end{aligned}$$

$$\begin{aligned}
P^{1Wi}_{2,par}\left(r\right) &= \frac{30\left(2+3\epsilon\right)\left(C^0_1\right)^2}{r^{10}} + \frac{50\left(59+78\epsilon\right)\left(C^0_1\right)^2}{7r^3} + \frac{75\left(72+143\epsilon\right)\left(C^0_1\right)^2 r^4}{14} \\
&- \frac{10\left(8+11\epsilon\right)C^0_1C^0_2}{r^8} - \frac{100\left(19+18\epsilon\right)C^0_1C^0_2}{7r^3} - \frac{25\left(23+36\epsilon\right)C^0_1C^0_2}{2r} \\
&- \frac{75\left(72+143\epsilon\right)C^0_1C^0_2 r^4}{7} + \frac{25\left(1+2\epsilon\right)\left(C^0_2\right)^2}{2r^6} - \frac{1250\left(1+2\epsilon\right)\left(C^0_2\right)^2}{7r^3} \\
&+ \frac{25\left(23+36\epsilon\right)\left(C^0_2\right)^2}{2r} + \frac{75\left(72+143\epsilon\right)\left(C^0_2\right)^2 r^4}{14}, \\
P^{1Wi}_{3,par}\left(r\right) &= \frac{\left(2+3\epsilon\right)\left(C^0_1\right)^2}{r^{10}} - \frac{5\left(59+78\epsilon\right)\left(C^0_1\right)^2}{7r^3} - \frac{735\left(1+2\epsilon\right)\left(C^0_1\right)^2 r^2}{4} \\
&+ \frac{5\left(1089+2120\epsilon\right)\left(C^0_1\right)^2 r^4}{112} + \frac{10\left(19+18\epsilon\right)C^0_1C^0_2}{7r^3} + \frac{10\left(3+5\epsilon\right)C^0_1C^0_2}{r} \\
&+ \frac{805\left(1+2\epsilon\right)C^0_1C^0_2 r^2}{2} - \frac{5\left(1089+2120\epsilon\right)C^0_1C^0_2 r^4}{56} \\
&+ \frac{125\left(1+2\epsilon\right)\left(C^0_2\right)^2}{7r^3} - \frac{10\left(3+5\epsilon\right)\left(C^0_2\right)^2}{r} - \frac{875\left(1+2\epsilon\right)\left(C^0_2\right)^2 r^2}{4} \\
&+ \frac{5\left(1089+2120\epsilon\right)\left(C^0_2\right)^2 r^4}{112}, \\
P^{1Wi}_{4,par}\left(r\right) &= 0,
\end{aligned} \tag{A.21}$$

all of which depend on the $O(1)$ constants C^0_1 and C^0_2 found in section 3.1.

Substitution of the boundary conditions allows us to solve for all the unknown constants in terms of the cell radius b; the solutions are identical to those for fully rigid spheres (as we have not yet accounted for deformability) and will not be given here as they are available in Escott and Wilson (2020).

Appendix B. Asymptotic expansions at order Ca_e

The scalar radial functions in the fluid phase, introduced in equations (58–61) obey governing equations (from the mass conservation, pressure Laplacian and momentum equations) which can be written in generic form as

$$\alpha^{1,1Ca_e}_{ij} V^{1Ca_e\prime}_j\left(r\right) + \frac{\beta^{1,1Ca_e}_{ij} V^{1Ca_e}_j\left(r\right)}{r} = 0, \tag{B.1}$$

$$P^{1Ca_e\prime\prime}_i\left(r\right) + \frac{2P^{1Ca_e\prime}_i\left(r\right)}{r} + \frac{\alpha^{2,1Ca_e}_{ij} P^{1Ca_e}_j\left(r\right)}{r^2} = 0, \tag{B.2}$$

$$V_i^{1\mathit{Ca}_{\mathrm{e}}\prime\prime}(r) + \frac{2V_i^{1\mathit{Ca}_{\mathrm{e}}\prime}(r)}{r} + \frac{\alpha_{ij}^{3,1\mathit{Ca}_{\mathrm{e}}} V_j^{1\mathit{Ca}_{\mathrm{e}}}(r)}{r^2} - \beta_{ij}^{2,1\mathit{Ca}_{\mathrm{e}}} P_j^{1\mathit{Ca}_{\mathrm{e}}\prime}(r) + \frac{\gamma_{ij}^{1,1\mathit{Ca}_{\mathrm{e}}} P_j^{1\mathit{Ca}_{\mathrm{e}}}(r)}{r} = 0. \quad \text{(B.3)}$$

For the solid phase equations, we repeat equation (B.1) but for $\overline{V}^{1\mathit{Ca}_{\mathrm{e}}}$. The remaining governing equations become

$$\begin{aligned} H_1^{0\prime\prime}(r) + \frac{2H_1^{0\prime}(r)}{r} + \frac{2\left(2H_2^0(r) - H_1^0(r)\right)}{r^2} - \frac{2L_1^0(r)}{r} &= 0, \\ H_2^{0\prime\prime}(r) + \frac{2H_2^{0\prime}(r)}{r} - \frac{12H_2^0(r)}{r^2} - L_1^{0\prime}(r) + \frac{2L_1^0(r)}{r} &= 0, \\ H_3^{0\prime\prime}(r) + \frac{2H_3^{0\prime}(r)}{r} - \frac{2H_3^0(r)}{r^2} &= 0, \end{aligned} \quad \text{(B.4)}$$

and (from the strain tensor evolution equation (36)):

$$\begin{aligned} \frac{\alpha_{ij}^{3,1\mathit{Ca}_{\mathrm{e}}} \overline{V}_j^{1\mathit{Ca}_{\mathrm{e}}}(r) - \alpha_{ij}^{4,1\mathit{Ca}_{\mathrm{e}}} H_j^{1\mathit{Ca}_{\mathrm{e}}}(r)}{r} &= 0, \\ \alpha_{ij}^{5,1\mathit{Ca}_{\mathrm{e}}} \overline{V}_j^{1\mathit{Ca}_{\mathrm{e}}\prime}(r) - \alpha_{ij}^{6,1\mathit{Ca}_{\mathrm{e}}} H_j^{1\mathit{Ca}_{\mathrm{e}}\prime}(r) + \frac{\beta_{ij}^{3,1\mathit{Ca}_{\mathrm{e}}} \overline{V}_j^{1\mathit{Ca}_{\mathrm{e}}}(r) - \beta_{ij}^{4,1\mathit{Ca}_{\mathrm{e}}} H_j^{1\mathit{Ca}_{\mathrm{e}}}(r)}{r} &= 0. \end{aligned} \quad \text{(B.5)}$$

The radial functions which solve equations (B.1)–(B.3) are, but for a change of constants, the same as the homogeneous solutions from (A.2–A.13); the solutions for the solid displacement and Lagrange pressure are new at this order. The solution forms are:

$$\begin{aligned} &\overline{V}_1^{1\mathit{Ca}_{\mathrm{e}}}(r) = 0, \quad \overline{V}_2^{1\mathit{Ca}_{\mathrm{e}}}(r) = 0, \quad \overline{V}_3^{1\mathit{Ca}_{\mathrm{e}}}(r) = 0, \quad \overline{V}_4^{1\mathit{Ca}_{\mathrm{e}}}(r) = 0, \\ &\overline{V}_5^{1\mathit{Ca}_{\mathrm{e}}}(r) = 0, \quad \overline{V}_6^{1\mathit{Ca}_{\mathrm{e}}}(r) = \frac{8\overline{C}_2^{1\mathit{Ca}_{\mathrm{e}}} r^3}{7} + \frac{2\overline{C}_3^{1\mathit{Ca}_{\mathrm{e}}}}{r^4}, \quad \overline{V}_7^{1\mathit{Ca}_{\mathrm{e}}}(r) = 0, \\ &\overline{V}_8^{1\mathit{Ca}_{\mathrm{e}}}(r) = \overline{C}_1^{1\mathit{Ca}_{\mathrm{e}}} r - \frac{10\overline{C}_2^{1\mathit{Ca}_{\mathrm{e}}} r^3}{7} - \frac{2\overline{C}_3^{1\mathit{Ca}_{\mathrm{e}}}}{5r^4} + \frac{7\overline{C}_3^{1\mathit{Ca}_{\mathrm{e}}} r}{5} + \overline{C}_5^{1\mathit{Ca}_{\mathrm{e}}} r, \\ &\overline{V}_9^{1\mathit{Ca}_{\mathrm{e}}}(r) = -\overline{C}_1^{1\mathit{Ca}_{\mathrm{e}}} r + \frac{10\overline{C}_2^{1\mathit{Ca}_{\mathrm{e}}} r^3}{7} + \frac{2\overline{C}_3^{1\mathit{Ca}_{\mathrm{e}}}}{5r^4} - \frac{7\overline{C}_3^{1\mathit{Ca}_{\mathrm{e}}} r}{5} + \overline{C}_5^{1\mathit{Ca}_{\mathrm{e}}} r, \\ &\quad H_1^0(r) = \overline{C}_1^{1\mathit{Ca}_{\mathrm{e}}} r - \frac{10\overline{C}_2^{1\mathit{Ca}_{\mathrm{e}}} r^3}{7} - \frac{2\overline{C}_3^{1\mathit{Ca}_{\mathrm{e}}}}{5r^4} + \frac{7\overline{C}_3^{1\mathit{Ca}_{\mathrm{e}}} r}{5}, \quad H_2^0(r) = \frac{4\overline{C}_2^{1\mathit{Ca}_{\mathrm{e}}} r^3}{7} + \frac{\overline{C}_3^{1\mathit{Ca}_{\mathrm{e}}}}{r^4}, \\ &\quad H_3^0(r) = \overline{C}_4^{1\mathit{Ca}_{\mathrm{e}}} r, \quad L_1^0(r) = -3\overline{C}_2^{1\mathit{Ca}_{\mathrm{e}}} r^2. \end{aligned} \quad \text{(B.6)}$$

We leave $C_{24}^{1\mathit{Ca}_{\mathrm{e}}}$ as a free parameter; $\overline{C}_4^{1\mathit{Ca}_{\mathrm{e}}}$ is also unsolved at this order, as neither is required to fully solve the equations and boundary conditions. Where necessary, when plotting solutions, we set either of them to zero.

The remaining constants are summarised as:

$$C_i^{1Ca_\mathrm{e}} = \frac{\mu_i^{1Ca_\mathrm{e}}\left(b\right)}{\kappa_i^{1Ca_\mathrm{e}}\left(b\right)} + \frac{\left(b^3\delta_{i,16} - \delta_{i,15} + b^3\delta_{i,18} - \delta_{i,17}\right)}{\left(b-1\right)\left(1+b+b^2\right)}\overline{C}_5^{1Ca_\mathrm{e}}, \tag{B.7}$$

given denominator functions κ^{1Ca_e}:

$$\begin{aligned}
\kappa_1^{1Ca_\mathrm{e}}\left(b\right) &= \kappa_2^{1Ca_\mathrm{e}}\left(b\right) = \kappa_7^{1Ca_\mathrm{e}}\left(b\right) = \kappa_8^{1Ca_\mathrm{e}}\left(b\right) = \kappa_{19}^{1Ca_\mathrm{e}}\left(b\right) = \kappa_{20}^{1Ca_\mathrm{e}}\left(b\right) \\
&= \left(b-1\right)^2\big(4 + 16b + 40b^2 + 80b^3 + 140b^4 + 224b^5 + 336b^6 + 399b^7 \\
&\qquad + 336b^8 + 224b^9 + 140b^{10} + 80b^{11} + 40b^{12} + 16b^{13} + 4b^{14}\big), \\
\kappa_3^{1Ca_\mathrm{e}}\left(b\right) &= \kappa_4^{1Ca_\mathrm{e}}\left(b\right) = \left(4 + 16b + 40b^2 + 55b^3 + 40b^4 + 16b^5 + 4b^6\right)\kappa_1^{1Ca_\mathrm{e}}\left(b\right), \\
\kappa_5^{1Ca_\mathrm{e}}\left(b\right) &= \kappa_6^{1Ca_\mathrm{e}}\left(b\right) = \kappa_9^{1Ca_\mathrm{e}}\left(b\right) = \kappa_{21}^{1Ca_\mathrm{e}}\left(b\right) = \kappa_{22}^{1Ca_\mathrm{e}}\left(b\right) = \left(b-1\right)^2\big(4 + 16b \\
&\qquad + 40b^2 + 55b^3 + 40b^4 + 16b^5 + 4b^6\big), \\
\kappa_{11}^{1Ca_\mathrm{e}}\left(b\right) &= \kappa_{12}^{1Ca_\mathrm{e}}\left(b\right) = \kappa_{15}^{1Ca_\mathrm{e}}\left(b\right) = \kappa_{17}^{1Ca_\mathrm{e}}\left(b\right) = \kappa_{25}^{1Ca_\mathrm{e}}\left(b\right) = \kappa_{26}^{1Ca_\mathrm{e}}\left(b\right) \\
&= \left(b-1\right)\kappa_5^{1Ca_\mathrm{e}}\left(b\right).
\end{aligned} \tag{B.8}$$

and numerator functions:

$$\begin{aligned}
\mu_i^{1Ca_\mathrm{e}}\left(b\right) = {} & \left(231C_1^0 - 265C_2^0\right)\left(7C_1^0 - 5C_2^0\right)\nu_i^{1,1Ca_\mathrm{e}}\left(b\right) \\
& + C_1^0\nu_i^{2,1Ca_\mathrm{e}}\left(b\right) + C_2^0\nu_i^{3,1Ca_\mathrm{e}}\left(b\right);
\end{aligned} \tag{B.9}$$

in which the coefficients ν_1^i and ν_2^i given explicitly in Escott (2021) and in the supplementary files. Within the solid phase, our constants $\overline{C}^{1Ca_\mathrm{e}}$ are small enough to write explicitly:

$$\begin{aligned}
\overline{C}_1^{1Ca_\mathrm{e}} &= \frac{5}{68}\left(441C_1^0 - 475C_2^0\right) \\
&= \frac{5b^3\left(475 + 475b + 34b^2 + 34b^3 + 34b^4 + 34b^5 + 34b^6\right)}{17(b-1)^3\left(4 + 16b + 40b^2 + 55b^3 + 40b^4 + 16b^5 + 4b^6\right)}, \\
\overline{C}_2^{1Ca_\mathrm{e}} &= \frac{1225}{68}\left(C_1^0 - C_2^0\right) \\
&= \frac{1225b^3\left(1+b\right)}{17(b-1)^3\left(4 + 16b + 40b^2 + 55b^3 + 40b^4 + 16b^5 + 4b^6\right)}, \\
\overline{C}_3^{1Ca_\mathrm{e}} &= 0,
\end{aligned} \tag{B.10}$$

along with the shape function $\rho_1^{1Ca_\mathrm{e}}$ which was given in equation (63).